Submitted 000 (2026) 000000

Dynamic homogenization and emergent bianisotropy in thermoelasticity

Gal Shmuel[a,b,*], John R. Willis[c]

[a] *Faculty of Mechanical Engineering, Technion–Israel Institute of Technology, Haifa, Israel*
[b] *Photonics Initiative, Advanced Science Research Center, City University of New York, New York, New York, USA*
[c] *Department of Applied Mathematics and Theoretical Physics, Centre for Mathematical Sciences, University of Cambridge, Cambridge, United Kingdom*

ARTICLE INFO

Article history:
Received 00 Month 2026
Revised 00 Month 2026
Accepted 00 Month 2026
Available online 00 Month 2026

Keywords:
Dynamic homogenization
Thermoelasticity
Metamaterials
Effective properties
Wave propagation
Bianisotropy
Willis couplings

ABSTRACT

We formulate a theory for the macroscopic response of heterogeneous thermoelastic media. The formulation employs independent driving fields and a Green-function representation, yielding exact nonlocal constitutive relations between the effective fields. Our theory predicts emergent cross-couplings between the elastic and thermal fields that are absent from the microscopic constitutive relations. We show that spatial inversion determines which of these couplings are permitted in the local limit, while spatial dispersion can retain inversion-odd couplings. For periodic laminates, a Fourier implementation shows that the effective model reproduces both acoustic-like and thermal-like Bloch dynamics, and that the emergent mixed couplings can strongly modify acoustic attenuation by altering the thermoelastic polarization of the modes. Finally, a generalized thermoelastic impedance reveals orientation-dependent thermoelastic conversion. Our framework provides a general homogenization route for uncovering emergent cross-couplings in other heterogeneous systems where propagating and diffusive fields coexist.

1. Introduction

Heterogeneous materials exhibit rich dynamics owing to multiple scattering, interference, and other microscale wave phenomena (Hussein et al., 2014). These dynamics are described by partial differential equations with spatially varying coefficients. Homogenization theories aim to replace this complex description with a fictitious homogeneous medium characterized by effective constitutive relations between suitably averaged fields (Milton, 2002; Srivastava, 2015). In doing so, homogenized models may expose macroscopic phenomena that are obscured by microscale field variations and the interplay of multiple spatial scales.

Many classical homogenization methods rely on asymptotic expansions and an assumed separation between microscopic and macroscopic length scales (Bensoussan et al., 2011; Nassar et al., 2016). Willis (1981, 1985, 1997, 2011) devised a fundamentally different approach to elastodynamic homogenization that does not require such scale separation (Meng and Guzina, 2018). A striking outcome of this approach is the emergence of anomalous cross-couplings between stress and velocity and between momentum and strain, now known as Willis couplings, analogous to bianisotropy in electromagnetism (Milton et al., 2006; Sieck et al., 2017). Since the introduction of this theory, substantial progress has been made in analyzing its mathematical structure (Nassar et al., 2015, 2016), elucidating the physical origin and implications of the effective couplings (Sieck et al., 2017), and demonstrating their consequences experimentally (Melnikov et al., 2019; Liu et al., 2019). One of the central developments that helped advance the field has been its local representation, commonly referred to as the Milton–Briane–Willis form (Milton et al., 2006; Milton, 2007; Milton).

The Willis couplings exemplify the metamaterial character of heterogeneous media, whereby homogenization reveals effective responses that are absent from, or qualitatively different from, those of the constituent materials (Kadic et al., 2013, 2019; Li et al.,

[1]Corresponding author. *E-mail address:* meshmuel@technion.ac.il (G. Shmuel).
E-mail address: jrw1005@cam.ac.uk (J.R. Willis).

2021). This raises the question of whether such architectured bianisotropic response can emerge more generally in heterogeneous media governed by other physical processes.

Indeed, extensions of Willis-type homogenization beyond elastodynamics have revealed analogous architectured couplings in other physical systems. Pernas-Salomón and Shmuel (2020b) generalized the framework to piezoelectric composites, where it revealed an effective coupling between momentum and electric field, termed electromomentum coupling (Pernas-Salomón and Shmuel, 2020a; Pernas-Salomón et al., 2021; Muhafra et al., 2023). Shmuel and Willis (2025, 2026a) subsequently adapted the same approach to heat conduction and identified thermal bianisotropy, namely, effective cross-couplings between heat flux and temperature and between entropy and temperature gradient Wu et al., which had previously been thought to require spatiotemporal modulation (Torrent et al., 2018; Xu et al., 2022). These developments demonstrate that Willis-type constitutive couplings arise more generally when distinct physical fields interact in heterogeneous media. Figure 1 schematically summarizes this perspective, illustrating how homogenization replaces microscopic heterogeneity by an effective medium whose constitutive architecture may contain couplings absent from the constituent materials.

These developments raise a natural question when propagating and diffusive fields coexist: what additional constitutive interactions are generated by heterogeneity between the two sectors? Thermoelasticity provides a canonical setting in which to address this question, since elastic-wave propagation and thermal diffusion are coupled already at the microscopic level through conventional thermoelasticity (Biot, 1956). We presented a concise account of the resulting concept of multiphysics bianisotropy and its observable scattering signatures in our companion Letter (Shmuel and Willis, 2026b). There, the theory was introduced to establish the emergence of wave–diffusion cross-couplings, while the physical demonstration focused primarily on a scattering-equivalent description of finite thermoelastic laminates and the resulting directional cross-channel conversion. Here, we provide the full theoretical development and use it to analyze in depth the bulk effective response of periodic media. We derive the exact source-driven constitutive operator for general heterogeneous thermoelastic media and its explicit Fourier representation for periodic composites, establish its reciprocity, symmetry, and spatial nonlocality properties, and determine how the emergent couplings modify the complex thermoelastic wave–diffusion spectrum and attenuation. We further connect the bulk theory to an observable boundary response through a scattering problem between a semi-infinite effective thermoelastic medium and a homogeneous elastic medium, thereby relating the emergent constitutive couplings directly to generalized thermoelastic impedance and thermomechanical conversion.

The resulting effective constitutive operator is considerably richer than that of standard thermoelasticity. In addition to the conventional couplings, it contains the Willis couplings, the thermal-bianisotropic couplings, and three reciprocal mixed pairs $\widetilde{\boldsymbol{\alpha}}$, $\widetilde{\boldsymbol{\gamma}}$, and $\widetilde{\boldsymbol{\Gamma}}$ that connect the propagating mechanical and diffusive thermal sectors. These mixed terms constitute a multiphysics bianisotropy of the effective thermoelastic medium.

We establish the spatial-symmetry and low-frequency structure of these couplings (Peng et al., 2022; Yves et al., 2026). In particular, $\widetilde{\boldsymbol{\alpha}}$ and $\widetilde{\boldsymbol{\Gamma}}$ are inversion odd, whereas $\widetilde{\boldsymbol{\gamma}}$ is inversion even. Hence, centrosymmetry eliminates the spatially local parts of the former couplings but not the latter. Importantly, this does not imply that the inversion-odd couplings vanish altogether: finite-wavenumber spatial dispersion can retain them in a centrosymmetric medium (Fietz and Shvets, 2010; Norris et al., 2012). The distinction separates bianisotropy produced locally by microscopic symmetry breaking from nonlocal coupling generated at finite wavelength.

The spatially local equations further show that the mixed couplings are not merely an alternative parametrization of conventional thermoelasticity. The coefficient $\widetilde{\boldsymbol{\alpha}}$ introduces temperature-curvature and strain-gradient terms, $\widetilde{\boldsymbol{\gamma}}$ modifies the conventional rate-dependent thermoelastic interaction, and $\widetilde{\boldsymbol{\Gamma}}$ introduces a zero-order mechanical–thermal coupling. By contrast, the mechanical Willis and thermal-bianisotropic pairs cancel from the local source-free bulk equations, although they remain present in boundary relations (Muhlestein et al., 2017; Sieck et al., 2017; Pernas-Salomón et al., 2021; Shmuel and Willis, 2025). This motivates a generalized thermoelastic modal impedance whose off-diagonal components quantify conversion between mechanical and thermal channels.

Although we employ thermoelasticity as a representative wave–diffusion system, our construction is not specific to it. The same source-driven homogenization procedure applies more generally once the appropriate kinetic and kinematic states, constitutive operator, and balance operators are identified. From this perspective, previously developed Willis-type homogenization theories can be recovered as particular cases of the present general derivation, obtained by restricting the state variables, constitutive structure, and balance laws to the corresponding setting (Willis, 2011; Pernas-Salomón and Shmuel, 2020b; Shmuel and Willis, 2026a). The present formulation further suggests that analogous effective cross-couplings should arise in other heterogeneous systems in which propagating and diffusive fields coexist and interact, including ionic media and piezoelectric semiconductors (Sagotra et al., 2019; Brenner et al., 2020; Hutson and White, 1962). More generally, the results illustrate how homogenization can strip away microscopic detail to expose a macroscopic mechanism: broken microscopic symmetry permits new constitutive interactions, these interactions modify coupled wave–diffusion dynamics and impedance, and their consequences can be isolated in measurable macroscopic response.

The remainder of the paper is organized as follows. Section 2 formulates the heterogeneous thermoelastic problem and introduces the operator notation used throughout the analysis. Section 3 develops the Green-function representation and the associated adjoint and reciprocity structure. Section 4 uses this representation to derive the exact source-driven effective constitutive relations for heterogeneous thermoelastic media. Section 5 analyzes the resulting effective operator, including the symmetry and spatial-nonlocality properties of the emergent couplings, the spatially local governing equations and generalized thermoelastic impedance, and the Fourier Schur-complement formulation for periodic media. Section 6 presents numerical examples that validate the effective model against the exact heterogeneous Bloch spectrum, quantify coupling-controlled acoustic

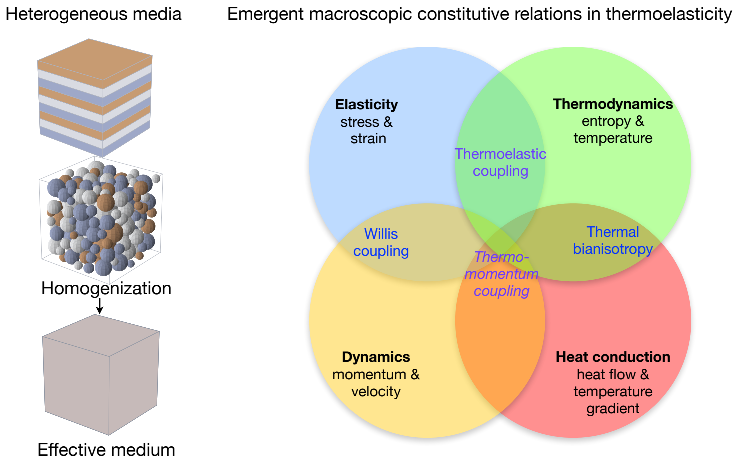

Fig. 1. Schematic illustration of dynamic homogenization and the resulting constitutive architecture. Heterogeneous media, whether periodic or random, are replaced by a homogeneous effective medium whose averaged fields are related through effective constitutive properties. In coupled thermoelastic dynamics, the effective description combines the conventional sectors of elasticity, dynamics, thermodynamics, and heat conduction. Their intersections contain the classical thermoelastic coupling, the Willis coupling between elastic and dynamic fields, thermal bianisotropy between thermodynamic and heat-conduction fields, and the multiphysics bianisotropic couplings between the elastic and thermal sectors studied here.

attenuation, examine the role of spatial symmetry, and demonstrate an observable impedance signature in a canonical scattering problem. We conclude this paper with a summary and discussion of our main results in Sec. 7.

2. Problem formulation

The composite has constitutive relations

$$\boldsymbol{\sigma} = \mathbf{C}\nabla\mathbf{u} - \boldsymbol{\beta}\theta, \quad \mathbf{p} = \rho\dot{\mathbf{u}}, \quad -\mathbf{q} = \boldsymbol{\kappa}\nabla\theta, \quad \theta_R\eta = \boldsymbol{\beta}^\eta\nabla\mathbf{u} + c\theta, \tag{1}$$

where $\boldsymbol{\sigma}$ is Cauchy stress, $\mathbf{p}$ is momentum density, $\mathbf{q}$ is the heat flux vector, η is the entropy density and θ_R is the reference temperature. Particle displacement is $\mathbf{u}$, velocity is $\dot{\mathbf{u}}$, and the asbsolute temperature is $\theta_R + \theta$. The elastic constant tensor $\mathbf{C}$ has components C_{jilk} which usually display the symmetries $C_{jilk} = C_{ijlk} = C_{klij}$, and the coupling tensors $\boldsymbol{\beta}$ and $\boldsymbol{\beta}^\eta$ have components β_{ji} and β^η_{ji}, respectively. Usually, $\boldsymbol{\beta}^\eta = \theta_R\boldsymbol{\beta}^\mathsf{T}$. However, these symmetries are not assumed in the derivations to follow, partly because the structure of the reasoning is more clearly exposed and partly because, with suitable interpretations of the variables, the resulting equations could be applied directly to a small perturbation of a pre-stressed nonlinear thermoelastic body, with $\mathbf{x}$ now denoting position in the undeformed configuration.

The body occupies a domain Ω and is subjected to body force $\mathbf{f}$ per unit volume and heat source density r. At each point of its boundary $\partial\Omega$, one of the pair $(n_j\sigma_{ji}, u_i)$ and one of the pair (n_jq_j, θ) are prescribed. It is assumed also that $\mathbf{u}$ and θ are zero for all times $t < 0$. For $t > 0$, the response is governed by the equation of motion

$$\nabla\cdot\boldsymbol{\sigma} + \mathbf{f} = \dot{\mathbf{p}} \qquad (\partial_j\sigma_{ji} + f_i = \dot{p}_i) \tag{2}$$

and the heat flux equation

$$-\nabla\cdot\mathbf{q} + r = \theta_R\dot{\eta} \qquad (-\partial_jq_j + r = \theta_R\dot{\eta}). \tag{3}$$

Henceforth, equations are Laplace transformed with respect to time, which replaces the time derivative with the transform variable $s = -\delta + \mathrm{i}\omega$. Time-harmonic disturbances are obtained by taking $\delta = 0$, but generally for a stable state $\delta > 0$ corresponds to a temporal decay rate, while $f = \operatorname{Im} s/(2\pi)$ is the oscillation frequency. Throughout, transformed fields are interpreted with time dependence e^{st}. The following symbolic notation will be employed:

$$\mathsf{w} = \begin{pmatrix}\mathbf{u}\\ \theta\end{pmatrix}, \quad \mathsf{g} = \begin{pmatrix}\mathbf{f}\\ r\end{pmatrix}, \quad \mathsf{D}^\mathsf{T} = \begin{pmatrix}\nabla\cdot & -s & 0 & 0\\ 0 & 0 & \nabla\cdot & -s\end{pmatrix}, \quad \mathsf{h} = \begin{pmatrix}\boldsymbol{\sigma}\\ \mathbf{p}\\ -\mathbf{q}\\ \theta_R\eta\end{pmatrix}, \quad \mathsf{L} = \begin{pmatrix}\mathbf{C} & 0 & 0 & -\boldsymbol{\beta}\\ 0 & \rho & 0 & 0\\ 0 & 0 & \boldsymbol{\kappa} & 0\\ \boldsymbol{\beta}^\eta & 0 & 0 & c\end{pmatrix}, \quad \mathsf{B} = \begin{pmatrix}\nabla & 0\\ s & 0\\ 0 & \nabla\\ 0 & 1\end{pmatrix}. \tag{4}$$

Employing this notation, the constitutive relations (1) become

$$\mathsf{h} = \mathsf{L}\mathsf{B}\mathsf{w}, \tag{5}$$

and the balance equations (2) and (3) imply

$$\mathsf{D}^\mathsf{T}\mathsf{L}\mathsf{B}\mathsf{w} + \mathsf{g} = 0. \tag{6}$$

3. Representation employing Green's function

First, to motivate the approach, define, for any two vector functions of position w and z, the bilinear form

$$(\mathsf{w},\mathsf{z}) = \int_\Omega d\mathbf{x}\, \mathsf{w}^\mathsf{T}(\mathbf{x})\mathsf{z}(\mathbf{x}),\ \mathsf{z} = \begin{pmatrix}\mathbf{u}_\mathrm{a}\\ \theta_\mathrm{a}\end{pmatrix}. \tag{7}$$

Then, for any operator A taking square-integrable w to square-integrable Aw, the operator $\mathsf{A}^\dagger$ adjoint to A is defined so that

$$(\mathsf{A}^\dagger\mathsf{z},\mathsf{w}) = (\mathsf{z},\mathsf{Aw}). \tag{8}$$

For operators such as those in (4), further restrictions on w and z are required, which will be clarified below.

Take $\mathsf{A} = \mathsf{D}^\mathsf{T}\mathsf{LB}$ and $\mathsf{A}^\dagger = \mathsf{B}^\dagger\mathsf{L}^\mathsf{T}(\mathsf{D}^\mathsf{T})^\dagger$, where

$$\mathsf{B}^\dagger = \begin{pmatrix}-\nabla\cdot & s & 0 & 0\\ 0 & 0 & -\nabla\cdot & 1\end{pmatrix}, \qquad (\mathsf{D}^\mathsf{T})^\dagger = \begin{pmatrix}-\nabla & 0\\ -s & 0\\ 0 & -\nabla\\ 0 & -s\end{pmatrix}. \tag{9}$$

It follows, by use of the divergence theorem, that

$$(\mathsf{z},\mathsf{Aw}) = \int_{\partial\Omega} dS\Big[\mathbf{u}_\mathrm{a}^\mathsf{T}(\mathbf{n}^\mathsf{T}\boldsymbol{\sigma}) - \theta_\mathrm{a}\,\mathbf{n}^\mathsf{T}\mathbf{q}\Big] + \int_\Omega d\mathbf{x}\left[(\mathsf{D}^\mathsf{T})^\dagger\mathsf{z}\right]^\mathsf{T}\mathsf{L}(\mathsf{Bw}), \tag{10}$$

and

$$(\mathsf{A}^\dagger\mathsf{z},\mathsf{w}) = -\int_{\partial\Omega} dS\Big[\mathbf{u}^\mathsf{T}(\mathbf{n}^\mathsf{T}\boldsymbol{\sigma}_\mathrm{a}) - \theta\,\mathbf{n}^\mathsf{T}\mathbf{q}_\mathrm{a}\Big] + \int_\Omega d\mathbf{x}\,(\mathsf{Bw})^\mathsf{T}\mathsf{L}^\mathsf{T}\left[(\mathsf{D}^\mathsf{T})^\dagger\mathsf{z}\right]. \tag{11}$$

Here the kinetic fields associated with the adjoint problem are

$$\begin{pmatrix}\boldsymbol{\sigma}_\mathrm{a}\\ -\mathbf{q}_\mathrm{a}\end{pmatrix} = \begin{pmatrix}-\mathbf{C}^\mathsf{T}\nabla\mathbf{u}_\mathrm{a} - s(\boldsymbol{\beta}^\eta)^\mathsf{T}\theta_\mathrm{a}\\ -\boldsymbol{\kappa}^\mathsf{T}\nabla\theta_\mathrm{a}\end{pmatrix}. \tag{12}$$

Hence, explicitly,

$$(\mathsf{z},\mathsf{Aw}) - (\mathsf{A}^\dagger\mathsf{z},\mathsf{w}) = \int_{\partial\Omega} dS\Big[\mathbf{u}_\mathrm{a}^\mathsf{T}(\mathbf{n}^\mathsf{T}\boldsymbol{\sigma}) + \mathbf{u}^\mathsf{T}(\mathbf{n}^\mathsf{T}\boldsymbol{\sigma}_\mathrm{a}) - \theta_\mathrm{a}\,\mathbf{n}^\mathsf{T}\mathbf{q} - \theta\,\mathbf{n}^\mathsf{T}\mathbf{q}_\mathrm{a}\Big]. \tag{13}$$

If w satisfies (6) and z satisfies

$$\mathsf{A}^\dagger\mathsf{z} + \mathsf{g}_\mathrm{a} = 0, \qquad \mathsf{g}_\mathrm{a} = \begin{pmatrix}\mathbf{f}_\mathrm{a}\\ r_\mathrm{a}\end{pmatrix}, \tag{14}$$

then

$$\int_{\partial\Omega} dS\Big[\mathbf{u}_\mathrm{a}^\mathsf{T}(\mathbf{n}^\mathsf{T}\boldsymbol{\sigma}) + \mathbf{u}^\mathsf{T}(\mathbf{n}^\mathsf{T}\boldsymbol{\sigma}_\mathrm{a}) - \theta_\mathrm{a}(\mathbf{n}^\mathsf{T}\mathbf{q}) - \theta(\mathbf{n}^\mathsf{T}\mathbf{q}_\mathrm{a})\Big] = (\mathsf{g}_\mathrm{a},\mathsf{w}) - (\mathsf{z},\mathsf{g}). \tag{15}$$

Now suppose that $\mathsf{w}(\mathbf{x})$ is replaced by the Green's function $\mathsf{G}(\mathbf{x},\mathbf{x}')$, with body forcing term $\mathsf{I}\delta(\mathbf{x}-\mathbf{x}')$ together with homogeneous boundary conditions, and $\mathsf{z}(\mathbf{x})$ is replaced by $\mathsf{G}^\dagger(\mathbf{x},\mathbf{x}'')$, together with homogeneous boundary conditions. The identity (15) then gives

$$\mathsf{G}^\dagger(\mathbf{x}',\mathbf{x}'') = \mathsf{G}^\mathsf{T}(\mathbf{x}'',\mathbf{x}'). \tag{16}$$

Next, apply the identity (15) to w and $\mathsf{G}^\dagger$ to obtain the representation

$$\mathsf{w} = (\mathsf{G}^\dagger,\mathsf{g}) + \int_{\partial\Omega} dS\left\{(\mathsf{G}^\dagger)^\mathsf{T}\begin{pmatrix}\mathbf{n}^\mathsf{T}\boldsymbol{\sigma}\\ -\mathbf{n}^\mathsf{T}\mathbf{q}\end{pmatrix} + \mathsf{w}^\mathsf{T}\begin{pmatrix}\mathbf{n}^\mathsf{T}\mathbf{S}^\dagger\\ -\mathbf{n}^\mathsf{T}\mathbf{Q}^\dagger\end{pmatrix}\right\}, \tag{17}$$

where $\mathbf{S}^\dagger$ and $\mathbf{Q}^\dagger$ are defined as in (12), with $\mathsf{G}^\dagger$ replacing z.

4. Effective constitutive relations

The representation (17) will now be applied to the case of a randomly inhomogeneous medium, in which the constitutive tensor L depends on position $\mathbf{x}$ within a sample parametrized by $\zeta \in \mathcal{S}$, over which a probability measure p is defined. Then, for instance, the ensemble mean of L at $\mathbf{x}$ is

$$\langle \mathsf{L} \rangle (\mathbf{x}) \equiv \langle \mathsf{L}(\mathbf{x}, \zeta) \rangle = \int_{\mathcal{S}} \mathsf{L}(\mathbf{x}, \zeta)\, p(d\zeta). \tag{18}$$

In the simplest case, a relation is sought between the means $\langle \mathsf{h} \rangle$ and $\mathsf{B}\langle \mathsf{w} \rangle$ but, following Willis (2011) and Shmuel and Willis (2026a), the problem is generalized to that of relating $\langle \mathsf{h} \rangle$ to the weighted mean $\left\langle w^{(2)} \mathsf{w} \right\rangle$, where $\left\langle w^{(2)} \right\rangle = 1$. As discussed by Willis (2011), there is no unique solution; expressed differently, there is an equivalence class of effective relations. One particular representative effective relation will be found by artificially generalizing the relation in sample ζ to

$$\mathsf{h} = \mathsf{L}(\mathsf{B}\mathsf{w} - \mathsf{m}) \tag{19}$$

and seeking a corresponding effective relation

$$\langle \mathsf{h} \rangle = \widetilde{\mathsf{L}}\left(\mathsf{B}\left\langle w^{(2)} \mathsf{w} \right\rangle - \mathsf{m}\right), \tag{20}$$

where here and henceforth, a tilde denotes an effective constitutive property. The artificial field m has arbitrary dependence on $\mathbf{x}$ but is sure, that is, independent of sample ζ. Its introduction modifies Eq. (6) to

$$\mathsf{D}^{\mathsf{T}}\mathsf{L}(\mathsf{B}\mathsf{w} - \mathsf{m}) + \mathsf{g} = 0. \tag{21}$$

The domain Ω is assumed fixed and any boundary condition on w is taken to be sure. However, the body source g and any specified components of $\mathbf{n}^{\mathsf{T}}\boldsymbol{\sigma}$, $\mathbf{n}^{\mathsf{T}}\mathbf{q}$ on $\partial\Omega$ are assumed to be given in the form of a function that is sure, times a weight $w^{(1)}(\mathbf{x}, \zeta)$, with $\left\langle w^{(1)} \right\rangle = 1$. This allows, for instance, treatment of a porous medium for which no loading can be applied within the pores.

It is permissible to replace w by $\left\langle w^{(2)} \mathsf{w} \right\rangle$ in the integrand of (17) because any participating component is sure. Having made that replacement, that term in the surface integral can be replaced, employing (11), to give

$$\mathsf{w} = \left\langle w^{(2)} \mathsf{w} \right\rangle + \mathsf{G}\, w^{(1)} \left\{ \mathsf{g}, \begin{bmatrix} \mathbf{n}^{\mathsf{T}}\boldsymbol{\sigma} \\ -\mathbf{n}^{\mathsf{T}}\mathbf{q} \end{bmatrix} \right\} + \int_{\Omega} d\mathbf{x}\, \left(\mathsf{D}^{\mathsf{T}\dagger}\mathsf{G}^{\dagger}\right)^{\mathsf{T}} \mathsf{L}\left(\mathsf{B}\left\langle w^{(2)} \mathsf{w} \right\rangle - \mathsf{m}\right). \tag{22}$$

Notation has been changed slightly here, replacing $\mathsf{G}^{\dagger\mathsf{T}}$ by G, and now regarding G as an operator, so that

$$(\mathsf{G}\phi)(\mathbf{x}') = \int \mathsf{G}(\mathbf{x}', \mathbf{x})\, \phi(\mathbf{x}), \tag{23}$$

the integral being taken over whatever domain $\phi(\mathbf{x})$ is defined. It follows from (22) that formally,

$$\left\{ \mathsf{g}, \begin{bmatrix} \mathbf{n}^{\mathsf{T}}\boldsymbol{\sigma} \\ -\mathbf{n}^{\mathsf{T}}\mathbf{q} \end{bmatrix} \right\} = -\left\langle w^{(2)} \mathsf{G} w^{(1)} \right\rangle^{-1} \int_{\Omega} d\mathbf{x}\ \left\langle w^{(2)} \left(\mathsf{D}^{\mathsf{T}\dagger}\mathsf{G}^{\dagger}\right)^{\mathsf{T}} \mathsf{L} \right\rangle \left(\mathsf{B}\left\langle w^{(2)} \mathsf{w} \right\rangle - \mathsf{m}\right). \tag{24}$$

and then, with $\left(\mathsf{D}^{\mathsf{T}\dagger}\mathsf{G}^{\dagger}\right)^{\dagger}$ interpreted as the operator $\int d\mathbf{x}\, \left(\mathsf{D}^{\mathsf{T}\dagger}\mathsf{G}^{\dagger}\right)^{\mathsf{T}}(\mathbf{x}', \mathbf{x})$,

$$\mathsf{w} = \left\langle w^{(2)} \mathsf{w} \right\rangle - \mathsf{G} w^{(1)}\, \left\langle w^{(2)} \mathsf{G} w^{(1)} \right\rangle^{-1} \left\langle w^{(2)} \left(\mathsf{D}^{\mathsf{T}\dagger}\mathsf{G}^{\dagger}\right)^{\dagger} \mathsf{L} \right\rangle \left(\mathsf{B}\left\langle w^{(2)} \mathsf{w} \right\rangle - \mathsf{m}\right) + \left(\mathsf{D}^{\mathsf{T}\dagger}\mathsf{G}^{\dagger}\right)^{\dagger} \mathsf{L}\left(\mathsf{B}\left\langle w^{(2)} \mathsf{w} \right\rangle - \mathsf{m}\right). \tag{25}$$

In consequence, from Eq. (19),

$$\langle \mathsf{h} \rangle = \langle \mathsf{L}(\mathsf{B}\mathsf{w} - \mathsf{m}) \rangle = \widetilde{\mathsf{L}}\left(\mathsf{B}\left\langle w^{(2)} \mathsf{w} \right\rangle - \mathsf{m}\right), \tag{26}$$

where the nonlocal operator $\widetilde{\mathsf{L}}$ is

$$\widetilde{\mathsf{L}} = \langle \mathsf{L} \rangle - \left\langle \mathsf{L}\mathsf{B}\mathsf{G} w^{(1)} \right\rangle \left\langle w^{(2)} \mathsf{G} w^{(1)} \right\rangle^{-1} \left\langle w^{(2)} \left(\mathsf{D}^{\mathsf{T}\dagger}\mathsf{G}^{\dagger}\right)^{\dagger} \mathsf{L} \right\rangle + \left\langle \mathsf{L}\mathsf{B}\left(\mathsf{D}^{\mathsf{T}\dagger}\mathsf{G}^{\dagger}\right)^{\dagger} \mathsf{L} \right\rangle. \tag{27}$$

Equation (27) is formulated at the operator level and is independent of the particular physical interpretation assigned to h, w, L, D, and B. Different physical systems are obtained by specifying these states and operators accordingly, so that the same formula may be applied to other heterogeneous wave–diffusion systems. Previously developed Willis-type homogenization theories can likewise be recovered as particular or limiting cases of this equation, obtained by restricting the state variables, constitutive structure, and balance operators to the corresponding setting (Willis, 2011; Pernas-Salomón and Shmuel, 2020b; Shmuel and Willis, 2026a). For the thermoelastic system considered here, after setting $w^{(1)} = w^{(2)}$ and $\mathsf{m} = 0$, the general effective operator in Eq. (27) takes the form (Shmuel and Willis, 2026b)

$$\begin{pmatrix} \langle \boldsymbol{\sigma} \rangle \\ \langle \mathbf{p} \rangle \\ -\langle \mathbf{q} \rangle \\ \langle \theta_R \eta \rangle \end{pmatrix} = \begin{pmatrix} \widetilde{\mathbf{C}} & \widetilde{\mathbf{S}} & \widetilde{\boldsymbol{\alpha}} & -\widetilde{\boldsymbol{\beta}} \\ \widetilde{\mathbf{S}}^{\mathsf{T}} & \widetilde{\boldsymbol{\rho}} & \widetilde{\boldsymbol{\gamma}} & \widetilde{\boldsymbol{\Gamma}} \\ -\theta_R s\, \widetilde{\boldsymbol{\alpha}}^{\mathsf{T}} & -\theta_R s\, \widetilde{\boldsymbol{\gamma}}^{\mathsf{T}} & \widetilde{\boldsymbol{\kappa}} & s\, \widetilde{\boldsymbol{\xi}} \\ \theta_R\, \widetilde{\boldsymbol{\beta}}^{\mathsf{T}} & -\theta_R\, \widetilde{\boldsymbol{\Gamma}}^{\mathsf{T}} & \widetilde{\boldsymbol{\xi}}^{\mathsf{T}} & \widetilde{c} \end{pmatrix} \begin{pmatrix} \langle \nabla \mathbf{u} \rangle \\ \langle s\mathbf{u} \rangle \\ \langle \nabla \theta \rangle \\ \langle \theta \rangle \end{pmatrix}. \tag{28}$$

Here, $\widetilde{\mathbf{S}}$ and $\widetilde{\boldsymbol{\xi}}$ are the Willis coupling and thermal-bianisotropic couplings, respectively, while $\widetilde{\boldsymbol{\alpha}}$, $\widetilde{\boldsymbol{\gamma}}$, and $\widetilde{\boldsymbol{\Gamma}}$ constitute emergent mixed wave–diffusion couplings, which we refer to as multiphysics bianisotropy.

A few comments on the structure of the effective relations are in order. First, we recall that generally, the two-point kernel $\widetilde{\mathsf{L}}(\mathbf{x}, \mathbf{x}', s)$ acts on the macroscopic fields through integration over $\mathbf{x}'$. For the equal-weight choice above and the reciprocal underlying heterogeneous medium considered here, the reciprocity symmetries imposed on the microscopic thermoelastic constitutive tensors are inherited by the homogenized description: the effective constitutive operator is self-adjoint with respect to the spatial bilinear pairing in Eq. (7), with the adjoint defined by Eq. (8), in the same operator sense detailed by Pernas-Salomón and Shmuel (2020a) and Shmuel and Willis (2026a). Accordingly, the off-diagonal couplings form spatial-adjoint pairs. At the kernel level, this adjoint operation includes both tensor transpose and interchange of the spatial arguments $(\mathbf{x}, \mathbf{x}') \mapsto (\mathbf{x}', \mathbf{x})$; the transpose notation in Eq. (28) suppresses this exchange of arguments. Thus, if the underlying heterogeneous medium is nonreciprocal, Eq. (27) still defines an effective constitutive operator, but the corresponding off-diagonal blocks are generally independent rather than adjoint pairs.

In addition to its spatial nonlocality, $\widetilde{\mathsf{L}}$ is generally nonlocal in time. In the Laplace domain, this memory is encoded in its generally non-polynomial dependence on s; upon inverse Laplace transformation, it appears as a causal temporal convolution, implying that the effective medium generally possesses memory.

5. Analysis

We now analyze the structure and physical implications of the effective constitutive relations derived above. We first classify the emergent couplings according to spatial inversion symmetry and their leading low-frequency behavior, thereby identifying which terms require broken centrosymmetry and which may persist in centrosymmetric media. We then specialize the formulation to one-dimensional periodic composites and examine the spatially local limit, deriving the corresponding coupled thermoelastic field equations, dispersion relation, and generalized modal impedances. Finally, we develop a Fourier-based implementation of the source-driven homogenization for periodic media, in which the nonzero microscopic harmonics are eliminated to obtain the effective constitutive operator explicitly as a function of the independent wavenumber and frequency variables (k, s).

5.1. Spatial inversion and symmetry of the effective couplings

The structure of the effective operator in Eq. (27) is constrained by the spatial symmetries of the medium. We focus first on spatial inversion, since it provides a direct classification of the effective cross-couplings that emerge under homogenization. Let $\mathcal{P}$ denote the active inversion about an inversion center, with the origin chosen at that center, such that

$$\mathcal{P} : \mathbf{x} \mapsto -\mathbf{x}, \qquad \mathbf{Q} = -\mathbf{I}. \tag{29}$$

This operation transforms the physical medium and fields, not merely a passive relabelling of the coordinates. Under inversion, scalars, polar vectors, and true second-order tensors transform, respectively, as

$$\phi'(\mathbf{x}) = \phi(-\mathbf{x}), \qquad \mathbf{a}'(\mathbf{x}) = \mathbf{Q}\,\mathbf{a}(-\mathbf{x}) = -\mathbf{a}(-\mathbf{x}), \qquad \mathbf{A}'(\mathbf{x}) = \mathbf{Q}\,\mathbf{A}(-\mathbf{x})\mathbf{Q}^{\mathsf{T}} = \mathbf{A}(-\mathbf{x}). \tag{30}$$

Accordingly, θ and η are inversion-even scalars; $\mathbf{u}$, $\dot{\mathbf{u}}$, $\mathbf{p}$, $\mathbf{q}$, and $\nabla\theta$ are inversion-odd polar vectors; and $\nabla\mathbf{u}$ and $\boldsymbol{\sigma}$ are inversion-even true second-order tensors.

The inversion character of an effective constitutive kernel now follows without further dynamical assumptions: a kernel connecting fields of the same inversion character is even under inversion, whereas one connecting fields of opposite character is odd. This gives the classification in Table 1. In particular, $\widetilde{\mathbf{S}}$, $\widetilde{\boldsymbol{\alpha}}$, $\widetilde{\boldsymbol{\Gamma}}$, and $\widetilde{\boldsymbol{\xi}}$ are inversion odd, whereas $\widetilde{\mathbf{C}}$, $\widetilde{\rho}$, $\widetilde{\boldsymbol{\kappa}}$, $\widetilde{c}$, $\widetilde{\boldsymbol{\beta}}$, and $\widetilde{\boldsymbol{\gamma}}$ are inversion even. This classification is the direct thermoelastic extension of the parity argument for Willis media (Peng et al., 2022) and is consistent with the general symmetry classification of phononic constitutive couplings (Yves et al., 2026).

For a statistically homogeneous medium, translational invariance reduces the two-point dependence of the effective kernels to the separation $\mathbf{r} = \mathbf{x} - \mathbf{x}'$, so that $\widetilde{\mathsf{L}}(\mathbf{x}, \mathbf{x}', s) = \widetilde{\mathsf{L}}(\mathbf{r}, s)$, for which we define the spatial Fourier transform[1]

$$\widetilde{\mathsf{L}}(\mathbf{k}, s) = \int_{\mathbb{R}^d} \widetilde{\mathsf{L}}(\mathbf{r}, s) e^{-\mathrm{i}\mathbf{k}\cdot\mathbf{r}}\, d\mathbf{r}. \tag{31}$$

With abuse of notation, we retain the tilde to denote effective properties in both real and Fourier space, with the understanding that the arguments indicate which representation is being used.

The inversion classification can now be expressed directly in terms of the Fourier-domain effective operator. Let P_h and P_b denote the representations of inversion on the kinetic and kinematic state spaces, respectively. If the medium itself is centrosymmetric, invariance under $\mathcal{P}$ requires

$$\widetilde{\mathsf{L}}(\mathbf{k}, s) = \mathsf{P}_h\, \widetilde{\mathsf{L}}(-\mathbf{k}, s)\, \mathsf{P}_b^{-1}. \tag{32}$$

In the one-dimensional ordering used below, both parity operators reduce to

$$\mathsf{P}_h = \mathsf{P}_b = \mathrm{diag}(1, -1, -1, 1). \tag{33}$$

[1]The corresponding inverse transform is proportional to $e^{+\mathrm{i}\mathbf{k}\cdot\mathbf{r}}$. Accordingly, spatial Fourier modes are written with the convention $e^{+\mathrm{i}\mathbf{k}\cdot\mathbf{x}}$, and, in one dimension, $e^{\mathrm{i}kx}$.

Table 1. Spatial-inversion character of the effective thermoelastic coefficients. The fourth column refers to the transformation of the coefficient under inversion of the material. The fifth column gives the consequence at $\mathbf{k} = \mathbf{0}$ for a centrosymmetric medium. The last column records the leading low-frequency order obtained for the present unbiased, time-independent thermoelastic composites when the coefficient is not forbidden by spatial symmetry; it is not a statement about parity in s.

Property	Coupled fields	Tensor order	Inversion	Centrosym. $\mathbf{k} = \mathbf{0}$	$s \to 0$
$\widetilde{\mathbf{C}}$	$\boldsymbol{\sigma}$–$\nabla\mathbf{u}$	fourth order	even	allowed	$O(1)$
$\widetilde{\rho}$	$\mathbf{p}$–$\mathbf{v}$	second order	even	allowed	$O(1)$
$\widetilde{\boldsymbol{\kappa}}$	$-\mathbf{q}$–$\nabla\theta$	second order	even	allowed	$O(1)$
$\widetilde{c}$	$\theta_R\eta$–θ	scalar	even	allowed	$O(1)$
$\widetilde{\boldsymbol{\beta}}$	$\boldsymbol{\sigma}$–θ	second order	even	allowed	$O(1)$
$\widetilde{\mathbf{S}}$	$\boldsymbol{\sigma}$–$\mathbf{v}$	third order	odd	zero	$O(s)$
$\widetilde{\boldsymbol{\alpha}}$	$\boldsymbol{\sigma}$–$\nabla\theta$	third order	odd	zero	$O(1)$
$\widetilde{\boldsymbol{\gamma}}$	$\mathbf{p}$–$\nabla\theta$	second order	even	allowed	$O(s)$
$\widetilde{\boldsymbol{\Gamma}}$	$\mathbf{p}$–θ	vector	odd	zero	$O(s)$
$\widetilde{\boldsymbol{\xi}}$	$\theta_R\eta$–$\nabla\theta$	vector	odd	zero	$O(1)$

Equation (32) shows that an inversion-odd block $\widetilde{A}$ of a centrosymmetric medium satisfies

$$\widetilde{A}(-\mathbf{k}, s) = -\widetilde{A}(\mathbf{k}, s), \qquad \widetilde{A}(\mathbf{0}, s) = 0, \tag{34}$$

whereas an inversion-even block satisfies

$$\widetilde{A}(-\mathbf{k}, s) = \widetilde{A}(\mathbf{k}, s). \tag{35}$$

When the effective operator is regular about $\mathbf{k} = \mathbf{0}$, the corresponding expansions contain only odd and even powers of $\mathbf{k}$, respectively. Accordingly, $\widetilde{\mathbf{S}}$, $\widetilde{\boldsymbol{\alpha}}$, $\widetilde{\boldsymbol{\Gamma}}$, and $\widetilde{\boldsymbol{\xi}}$ vanish in the spatially local limit of a centrosymmetric medium, while they may remain nonzero at finite $\mathbf{k}$ through spatial dispersion. This distinction is important: centrosymmetry eliminates the *local* part of an inversion-odd coupling, not its entire nonlocal kernel. Peng et al. (2022) show that the local acoustic Willis coefficients vanish under parity and also that Willis phenomena can be represented through spatially nonlocal direct parameters. Equivalently, the Willis tensor of an inversion-symmetric phononic medium obeys an odd-wavevector constraint, and therefore vanishes only in its local $\mathbf{k} \to \mathbf{0}$ limit (Yves et al., 2026).

Broken centrosymmetry removes this constraint at $\mathbf{k} = \mathbf{0}$. Consequently, microscopic structural asymmetry appears in the homogenized description as a finite local value of an otherwise forbidden constitutive coupling. In this sense, spatial-symmetry breaking provides a direct route from microscopic heterogeneity to emergent macroscopic bianisotropy:

$$\begin{gathered}\text{broken microscopic centrosymmetry}\\ \downarrow\\ \text{symmetry-allowed local cross-couplings}\\ \downarrow\\ \text{emergent macroscopic bianisotropic response.}\end{gathered}$$

Centrosymmetry should not be confused with invariance under a single reflection except in one spatial dimension. In three dimensions, for example, reflection across the plane normal to $\mathbf{e}_1$ is represented by

$$\mathbf{Q}_{\mathrm{m}} = \mathrm{diag}(-1, 1, 1), \tag{36}$$

rather than by $-\mathbf{I}$. If such a reflection is a symmetry, the vector coupling $\widetilde{\boldsymbol{\Gamma}}$ obeys $\widetilde{\boldsymbol{\Gamma}} = \mathbf{Q}_{\mathrm{m}}\widetilde{\boldsymbol{\Gamma}}$ at $\mathbf{k} = \mathbf{0}$, which forces $\widetilde{\Gamma}_1 = 0$ but does not in general require $\widetilde{\Gamma}_2$ or $\widetilde{\Gamma}_3$ to vanish. Likewise, a component of the third-order tensor $\widetilde{\boldsymbol{\alpha}}$ is eliminated by this mirror only when its transformation acquires a minus sign; for the mirror (36), these are the components containing an odd number of indices equal to 1. Full inversion, by contrast, changes the sign of every component of an odd-rank polar tensor and therefore forces the entire inversion-odd tensor to vanish locally. Reflection and inversion coincide in the one-dimensional specialization considered below.

Finally, spatial inversion parity and low-frequency behavior are independent classifications. For the present time-independent, unbiased thermoelastic composites, the low-frequency expansion gives, when the corresponding term is permitted by spatial symmetry,

$$\widetilde{\mathbf{S}} = O(s), \qquad \widetilde{\boldsymbol{\alpha}} = O(1), \qquad \widetilde{\boldsymbol{\gamma}} = O(s), \qquad \widetilde{\boldsymbol{\Gamma}} = O(s), \qquad \widetilde{\boldsymbol{\xi}} = O(1). \tag{37}$$

The heat-flux–temperature partner of $\widetilde{\boldsymbol{\xi}}$ is $s\widetilde{\boldsymbol{\xi}}$ and therefore vanishes linearly with s. In particular, $\widetilde{\boldsymbol{\gamma}}$ is inversion even but tends to zero in the static limit. This is physically consistent with its constitutive role: it couples a temperature gradient to momentum density, whereas a stationary temperature gradient cannot sustain an equilibrium momentum density in the unbiased thermoelastic medium considered here. Similarly, $\widetilde{\boldsymbol{\Gamma}}$ is dynamically generated, whereas the stress–temperature-gradient coupling $\widetilde{\boldsymbol{\alpha}}$ can possess a finite static value once centrosymmetry is broken. None of these low-frequency statements implies, by itself, a global identity under $s \mapsto -s$; in particular, $\widetilde{\boldsymbol{\gamma}} = O(s)$ should not be interpreted as proof that $\widetilde{\boldsymbol{\gamma}}(-s) = -\widetilde{\boldsymbol{\gamma}}(s)$.

5.2. Local effective equations

In the source-free one-dimensional setting, the macroscopic balance equations are

$$\langle \sigma \rangle_{,x} - s \langle p \rangle = 0, \qquad (-\langle q \rangle)_{,x} - s\theta_R \langle \eta \rangle = 0. \tag{38}$$

Substituting the spatially local effective constitutive relations into Eq. (38) gives

$$\widetilde{C} \langle u \rangle_{,xx} - \widetilde{\rho} s^2 \langle u \rangle + \widetilde{\alpha} \langle \theta \rangle_{,xx} - (\widetilde{\beta} + s\widetilde{\gamma}) \langle \theta \rangle_{,x} - s\widetilde{\Gamma} \langle \theta \rangle = 0, \tag{39}$$

$$\widetilde{\kappa} \langle \theta \rangle_{,xx} - s\widetilde{c} \langle \theta \rangle - \theta_R s\widetilde{\alpha} \langle u \rangle_{,xx} - \theta_R s(\widetilde{\beta} + s\widetilde{\gamma}) \langle u \rangle_{,x} + \theta_R s^2 \widetilde{\Gamma} \langle u \rangle = 0, \tag{40}$$

where each tilded coefficient denotes its spatially local value $\widetilde{A}(0, s)$. The coefficients therefore have no explicit constitutive dependence on k, but generally retain their dependence on s and hence the temporal nonlocality of the effective medium.

By contrast, we recall that in standard thermoelasticity

$$Cu_{,xx} - \rho s^2 u - \beta\theta_{,x} = 0, \tag{41}$$

$$\kappa\theta_{,xx} - cs\theta - \theta_R \beta s u_{,x} = 0. \tag{42}$$

Examining Eqs. (39)-(40) in comparsion with Eqs. (41)-(42) shows that two reciprocal pairs cancel identically from these local bulk equations, namely, the Willis pair $\widetilde{S}$ and its thermal counterpart $\widetilde{\xi}$. (Nevertheless, they modify the impedance, which we analyze below.) The multiphysics bianisotropic terms, by contrast, remain. The coefficient $\widetilde{\alpha}$ generates a temperature-curvature term in the mechanical equation and a strain-gradient term in the thermal equation; $\widetilde{\gamma}$ enters through the rate-dependent combination $\widetilde{\beta} + s\widetilde{\gamma}$ and therefore modifies the conventional first-gradient thermoelastic coupling; and $\widetilde{\Gamma}$ introduces a spatially zero-order displacement–temperature coupling. The effective local bulk equations therefore cannot, in general, be reduced to standard thermoelasticity by merely renaming the conventional material constants.

It is useful to consider a spatial Fourier mode at fixed Laplace parameter s,

$$\langle u \rangle (x, s) = \widehat{u}\, e^{\mathrm{i}kx}, \qquad \langle \theta \rangle (x, s) = \widehat{\theta}\, e^{\mathrm{i}kx}, \tag{43}$$

so that spatial derivatives are replaced by products of $\mathrm{i}k$. Together with the temporal convention e^{st} adopted above, the spatial Fourier-mode convention $e^{\mathrm{i}kx}$ implies that, in the time-harmonic limit $s = \mathrm{i}\omega$, a mode has phase factor[2] $e^{\mathrm{i}(\omega t + kx)}$. Eqs. (39) and (40) then become

$$\mathsf{K}_{\mathrm{loc}}(k, s) \begin{pmatrix} \widehat{u} \\ \widehat{\theta} \end{pmatrix} = 0, \tag{44}$$

with

$$\mathsf{K}_{\mathrm{loc}}(k, s) = \begin{pmatrix} -\widetilde{C}k^2 - \widetilde{\rho}s^2 & -\widetilde{\alpha}k^2 - \mathrm{i}k(\widetilde{\beta} + s\widetilde{\gamma}) - s\widetilde{\Gamma} \\ \theta_R s\left[\widetilde{\alpha}k^2 - \mathrm{i}k(\widetilde{\beta} + s\widetilde{\gamma}) + s\widetilde{\Gamma}\right] & -\widetilde{\kappa}k^2 - \widetilde{c}s \end{pmatrix}, \tag{45}$$

so that $\mathsf{K}_{\mathrm{loc}}$ is the 2×2 source-free bulk operator acting on the displacement and temperature amplitudes. A nontrivial local mode requires

$$\det \mathsf{K}_{\mathrm{loc}}(k, s) = 0, \tag{46}$$

for which direct evaluation gives

$$\det \mathsf{K}_{\mathrm{loc}} = \left(-\widetilde{C}k^2 - \widetilde{\rho}s^2\right)\left(-\widetilde{\kappa}k^2 - \widetilde{c}s\right) + \theta_R s \left[\left(\widetilde{\alpha}k^2 + \widetilde{\Gamma}s\right)^2 + \left(\widetilde{\beta} + s\widetilde{\gamma}\right)^2 k^2\right]. \tag{47}$$

Its structure shows that the mixed couplings do not enter the modal problem as three independent modifications: $\widetilde{\alpha}$ and $\widetilde{\Gamma}$ appear through $\widetilde{\alpha}k^2 + \widetilde{\Gamma}s$, whereas $\widetilde{\gamma}$ modifies the apparent thermoelastic coupling through $\widetilde{\beta} + s\widetilde{\gamma}$. Accordingly, a free-wave spectrum alone cannot, in general, identify the individual constitutive properties.

Setting $\widetilde{\alpha} = \widetilde{\gamma} = \widetilde{\Gamma} = 0$ recovers the classical thermoelastic form with effective direct coefficients. Eqs. (41) and (42) are recovered when these coefficients are further specialized to the homogeneous constituent values C, ρ, κ, c, and β. In summary, dynamic homogenization predicts that macroscopically, there is a curvature–gradient conversion,$\widetilde{\alpha}$, a rate-dependent thermoelastic response, $\widetilde{\gamma}$, and a spatially zero-order thermomechanical conversion, $\widetilde{\Gamma}$.

[2] In a conventional positive-index medium with $\omega > 0$, phase propagation toward increasing x corresponds to $k < 0$. The physically admissible spatial roots are selected instead by the appropriate radiation or decay condition; in particular, a mode decaying into $x > 0$ satisfies $\mathrm{Im}\, k > 0$.

The same bulk modes define a generalized thermoelastic modal impedance. For a local Fourier mode, the constitutive relations give

$$\mathsf{t} = \mathsf{T}_{\mathrm{loc}}(k,s)\mathsf{w}, \text{ where } \quad \mathsf{t} = \begin{pmatrix}\sigma\\ q\end{pmatrix}, \quad \mathsf{T}_{\mathrm{loc}}(k,s) = \begin{pmatrix}\mathrm{i}k\widetilde{C} + s\widetilde{S} & \mathrm{i}k\widetilde{\alpha} - \widetilde{\beta}\\ \theta_R s\left(\mathrm{i}k\widetilde{\alpha} + s\widetilde{\gamma}\right) & -\mathrm{i}k\widetilde{\kappa} - s\widetilde{\xi}\end{pmatrix}. \tag{48}$$

So, although $\widetilde{S}$ and $\widetilde{\xi}$ cancel from the local bulk equations, they remain explicitly in the boundary variables. The matrix $\mathsf{T}_{\mathrm{loc}}$ by itself is not a scalar characteristic impedance, since the displacement and temperature components of a thermoelastic mode are coupled. For each spatial root k_j, let

$$\widehat{\mathsf{w}}_j = \begin{pmatrix}\widehat{u}_j\\ \widehat{\theta}_j\end{pmatrix}, \qquad r_j := \frac{\widehat{\theta}_j}{\widehat{u}_j}, \tag{49}$$

where $\widehat{\mathsf{w}}_j$ satisfies $\mathsf{K}_{\mathrm{loc}}(k_j,s)\widehat{\mathsf{w}}_j = 0$. Using the first row of this equation gives

$$r_j = -\frac{\widetilde{C}k_j^2 + \widetilde{\rho}s^2}{\widetilde{\alpha}k_j^2 + \mathrm{i}k_j\left(\widetilde{\beta} + s\widetilde{\gamma}\right) + s\widetilde{\Gamma}}, \tag{50}$$

whenever the denominator is nonzero. Thus both the wavenumber and the mechanical–thermal polarization are determined by the bulk eigenproblem before an impedance is assigned to the mode. The elastic characteristic impedance of mode j is naturally defined as stress divided by particle velocity,

$$Z_{u,j} := \frac{\widehat{\sigma}_j}{s\widehat{u}_j} = \widetilde{S} + \frac{\mathrm{i}k_j\widetilde{C}}{s} + \frac{\mathrm{i}k_j\widetilde{\alpha} - \widetilde{\beta}}{s} r_j. \tag{51}$$

Similarly, the thermal characteristic impedance is defined as temperature divided by heat flux,

$$Z_{\theta,j} := \frac{\widehat{\theta}_j}{\widehat{q}_j} = \left[\frac{\theta_R s\left(\mathrm{i}k_j\widetilde{\alpha} + s\widetilde{\gamma}\right)}{r_j} - \mathrm{i}k_j\widetilde{\kappa} - s\widetilde{\xi}\right]^{-1}. \tag{52}$$

Accordingly, the coupled thermoelastic medium possesses a displacement-channel and a temperature-channel impedance for each of its two spatial branches and for each propagation or decay direction. These scalar quantities describe a particular eigenmode; they do not by themselves characterize an arbitrary superposition of the two thermoelastic modes.

Equations (51) and (52) show how the emergent couplings modify the macroscopic characteristic impedances. The Willis coefficient $\widetilde{S}$, although absent from the local bulk dispersion relation, enters $Z_{u,j}$ directly, in agreement with previous studies (Sieck et al., 2017; Muhlestein et al., 2017; Pernas-Salomón et al., 2021). Likewise, $\widetilde{\xi}$ is absent from the local bulk dispersion relation but enters $Z_{\theta,j}$ directly (Shmuel and Willis, 2025, 2026a). The mixed coupling $\widetilde{\alpha}$ enters both impedances explicitly and also modifies them indirectly through k_j and r_j. The term $\widetilde{\gamma}$ enters $Z_{\theta,j}$ explicitly and $Z_{u,j}$ indirectly through the modal wavenumber and polarization. Finally, $\widetilde{\Gamma}$ does not appear explicitly in $\mathsf{T}_{\mathrm{loc}}$, because its constitutive pair couples temperature to momentum and velocity to entropy rather than directly to stress or heat flux. Nevertheless, it modifies both impedances through its effect on k_j and r_j.

These expressions recover the familiar one-field limits and make their low-frequency directional phase corrections explicit. Specifically, in the pure Willis limit with $s = \mathrm{i}\omega$, we define $C_0 := \widetilde{C}(0)$ and $\rho_0 := \widetilde{\rho}(0)$, and we have

$$Z_{u,\pm}(\omega) = \pm Z_{u,0} + \mathrm{i}\omega\widehat{S} + O(\omega^2), \quad Z_{u,0} := \sqrt{\rho_0 C_0}, \quad \widetilde{S}(\mathrm{i}\omega) = \mathrm{i}\omega\widehat{S} + O(\omega^2), \tag{53}$$

where the two signs label the opposite spatial roots. (With the convention specified above, these algebraic signs do not by themselves specify the physical propagation direction.) The thermal-only limit has the same underlying mechanism, although the diffusive relation between frequency and wavenumber introduces a square-root frequency dependence. Define $\kappa_0 := \widetilde{\kappa}(0)$, $c_0 := \widetilde{c}(0)$, where using $(\mathrm{i}\omega)^{1/2} = e^{\mathrm{i}\pi/4}\sqrt{\omega}$ gives

$$\widehat{Z}_{\theta,\pm}(\omega) = \pm\widehat{Z}_{\theta,0} + e^{\mathrm{i}\pi/4}\sqrt{\omega}\,\widehat{\xi}\,\widehat{Z}_{\theta,0}^2 + O(\omega), \qquad \widehat{Z}_{\theta,0} := \frac{1}{\sqrt{\kappa_0 c_0}}, \tag{54}$$

where $\widetilde{\xi}(\mathrm{i}\omega) = \widehat{\xi} + O(\omega)$ with real $\widehat{\xi}$.

The leading conventional normalized thermal impedances are therefore opposite real quantities, while the real bianisotropic coefficient $\widehat{\xi}$ generates the same complex modification to both. The factor $e^{\mathrm{i}\pi/4}$ originates from the diffusive relation $k_\theta \propto (\mathrm{i}\omega)^{1/2}$; hence the correction is not purely imaginary as in the mechanical Willis limit, but it likewise produces a direction-dependent phase.

For the fully coupled problem, a single scalar impedance cannot describe the response of an arbitrary superposition of the two admissible modes. For either radiation/decay subspace, collect the two modal potential vectors as

$$\mathsf{W}^{\pm} = \begin{pmatrix}| & |\\ \widehat{\mathsf{w}}_1^{\pm} & \widehat{\mathsf{w}}_2^{\pm}\\ | & |\end{pmatrix}, \tag{55}$$

and their corresponding boundary-flux vectors as

$$\mathsf{F}^{\pm} = \begin{pmatrix} | & | \\ \widehat{\mathsf{t}}_1^{\pm} & \widehat{\mathsf{t}}_2^{\pm} \\ | & | \end{pmatrix}, \qquad \widehat{\mathsf{t}}_j^{\pm} = \mathsf{T}_{\text{loc}}(k_j^{\pm}, s)\widehat{\mathsf{w}}_j^{\pm}. \tag{56}$$

The corresponding two-channel modal boundary map is

$$\mathsf{Z}^{\pm} = \mathsf{F}^{\pm}\left(\mathsf{W}^{\pm}\right)^{-1}. \tag{57}$$

Here the superscripts + and − label the radiation/decay subspaces admissible in the positive and negative half-spaces, respectively; they do not denote the algebraic sign of the corresponding wavenumber. This construction eliminates the arbitrary normalization of the individual eigenvectors. Its diagonal entries describe same-channel displacement and temperature boundary responses, whereas its off-diagonal entries quantify thermomechanical conversion.

In general, $\mathsf{Z}^{+} \neq \mathsf{Z}^{-}$ even for a reciprocal medium: reciprocity of the spatially local medium gives

$$\mathsf{R}_T\mathsf{Z}^{\pm} = \left(\mathsf{Z}^{\pm}\right)^{\mathsf{T}}\mathsf{R}_T, \qquad \mathsf{R}_T = \operatorname{diag}(s\theta_R, 1), \tag{58}$$

and hence

$$Z_{21}^{\pm} = s\theta_R Z_{12}^{\pm}. \tag{59}$$

Reciprocity therefore constrains each oriented modal boundary map but does not require the two orientations to coincide. Broken spatial inversion can consequently produce different displacement- and temperature-channel impedances, thermomechanical conversion, and reflection phases for opposite orientations while leaving the reciprocal bulk spectrum unchanged.

5.3. Fourier-based implementation

We now specialize the source-driven construction to a one-dimensional periodic medium and derive an explicit representation of the effective constitutive operator. The procedure is closely related to plane-wave-expansion homogenization: the periodic microscopic fields are expanded in Fourier space, the zero term is identified as the macroscopic field, and the nonzero harmonics are solved in terms of it and eliminated (Ponge et al., 2017; Pernas-Salomón and Shmuel, 2018; Muhafra et al., 2022). Introducing the residual sources as in Sec. 4 makes the effective kinematic variables algebraically independent, so that the elimination determines a constitutive operator for arbitrary (k, s) rather than only a source-free dispersion relation.

We begin by defining the period ℓ and introducing

$$G_n = \frac{2\pi n}{\ell}, \qquad K_n = k + G_n, \qquad n \in \mathbb{Z}. \tag{60}$$

With the convention

$$\mathsf{L}(x) = \sum_{p\in\mathbb{Z}} \mathsf{L}_p e^{\mathrm{i}G_p x}, \qquad \mathsf{L}_p = \frac{1}{\ell}\int_0^{\ell} \mathsf{L}(x)e^{-\mathrm{i}G_p x}\,dx, \tag{61}$$

We consider sources of the form

$$\mathsf{g}(x) = \mathsf{g}_0 e^{\mathrm{i}kx}, \quad \mathsf{m}(x) = \mathsf{m}_0 e^{\mathrm{i}kx}, \tag{62}$$

driving Bloch fields that can be expanded according to

$$\mathsf{w}(x) = e^{\mathrm{i}kx}\sum_{n\in\mathbb{Z}} \mathsf{w}_n e^{\mathrm{i}G_n x}, \qquad \mathsf{w}_n = \begin{pmatrix} u_n \\ \theta_n \end{pmatrix}. \tag{63}$$

The zero coefficient w_0 is the cell average of the periodic part of $\mathsf{w}(x)$, while $\mathsf{w}_{n\neq 0}$ describe the microscopic periodic fluctuations of displacement and temperature.

Acting on the nth harmonic, the differential operators are

$$\mathsf{B}_n = \begin{pmatrix} \mathrm{i}K_n & 0 \\ s & 0 \\ 0 & \mathrm{i}K_n \\ 0 & 1 \end{pmatrix}, \qquad \mathsf{D}_n^{\mathsf{T}} = \begin{pmatrix} \mathrm{i}K_n & -s & 0 & 0 \\ 0 & 0 & \mathrm{i}K_n & -s \end{pmatrix}. \tag{64}$$

We define the mean kinematic state by

$$\overline{\mathsf{b}} := \mathsf{B}_0\mathsf{w}_0 - \mathsf{m}_0, \tag{65}$$

in terms of which the complete microscopic kinematic argument of the constitutive law is

$$\mathsf{B}\mathsf{w} - \mathsf{m} = e^{\mathrm{i}kx}\left[\overline{\mathsf{b}} + \sum_{m\neq 0}\mathsf{B}_m\mathsf{w}_m e^{\mathrm{i}G_m x}\right]. \tag{66}$$

Similarly,

$$\overline{\mathsf{h}} := \mathsf{h}_0 = \mathsf{L}_0\overline{\mathsf{b}} + \sum_{m\neq 0} \mathsf{L}_{-m}\mathsf{B}_m\mathsf{w}_m. \tag{67}$$

Multiplication by the periodic constitutive matrix produces a convolution of Fourier coefficients. Hence the nth harmonic of the kinetic state is

$$\mathsf{h}_n = \mathsf{L}_n\overline{\mathsf{b}} + \sum_{m\neq 0} \mathsf{L}_{n-m}\mathsf{B}_m\mathsf{w}_m. \tag{68}$$

Equation (68) is the Fourier representation of the microscopic constitutive relation. Accordingly, for every $n \neq 0$, the Fourier component of the balance equations is

$$\mathsf{D}_n^{\mathsf{T}}\mathsf{h}_n = 0. \tag{69}$$

Thus, the microscopic fluctuation equations are

$$\sum_{m\neq 0} \mathsf{D}_n^{\mathsf{T}}\mathsf{L}_{n-m}\mathsf{B}_m\mathsf{w}_m = -\mathsf{D}_n^{\mathsf{T}}\mathsf{L}_n\overline{\mathsf{b}}, \qquad n \neq 0, \tag{70}$$

so that the 2×2 block multiplying w_m is

$$\mathsf{A}_{nm} := \mathsf{D}_n^{\mathsf{T}}\mathsf{L}_{n-m}\mathsf{B}_m = \begin{pmatrix} -C_{n-m}K_nK_m - \rho_{n-m}s^2 & -\mathrm{i}K_n\beta_{n-m} \\ -\mathrm{i}\theta_R sK_m\beta_{n-m} & -\kappa_{n-m}K_nK_m - c_{n-m}s \end{pmatrix}. \tag{71}$$

To proceed, it is useful to truncate the reciprocal lattice to $|n| \leq N$ and define

$$\mathcal{I}_N := \{-N, \ldots, -1, 1, \ldots, N\}, \tag{72}$$

so that stacking the $2N$ nonzero potential harmonics defines $\mathsf{W} \in \mathbb{C}^{4N}$, stacking $\{\mathsf{D}_n^{\mathsf{T}}\mathsf{L}_n\}$ defines $\mathsf{F} \in \mathbb{C}^{4N\times 4}$, and stacking $\{\mathsf{A}_{nm}\}$ defines $\mathsf{A} \in \mathbb{C}^{4N\times 4N}$. In terms of these matrices, the nonzero-harmonic equations take the compact form

$$\mathsf{A}\mathsf{W} = -\mathsf{F}\overline{\mathsf{b}}. \tag{73}$$

Whenever A is invertible,

$$\mathsf{W} = -\mathsf{A}^{-1}\mathsf{F}\overline{\mathsf{b}}. \tag{74}$$

Equations (73) and (67) can then be written together as

$$\begin{pmatrix} \overline{\mathsf{h}} \\ 0 \end{pmatrix} = \begin{pmatrix} \mathsf{L}_0 & \mathsf{C}_{\mathrm{f}} \\ \mathsf{F} & \mathsf{A} \end{pmatrix} \begin{pmatrix} \overline{\mathsf{b}} \\ \mathsf{W} \end{pmatrix}, \tag{75}$$

where

$$\mathsf{C}_{\mathrm{f}} := \begin{pmatrix} \mathsf{L}_N\mathsf{B}_{-N} & \cdots & \mathsf{L}_1\mathsf{B}_{-1} & \mathsf{L}_{-1}\mathsf{B}_1 & \cdots & \mathsf{L}_{-N}\mathsf{B}_N \end{pmatrix} \in \mathbb{C}^{4\times 4N}. \tag{76}$$

Eliminating W with Eq. (74) yields

$$\overline{\mathsf{h}} = \widetilde{\mathsf{L}}^{(N)}(k,s)\overline{\mathsf{b}}, \qquad \widetilde{\mathsf{L}}^{(N)} = \mathsf{L}_0 - \mathsf{C}_{\mathrm{f}}\mathsf{A}^{-1}\mathsf{F} = \mathsf{L}_0 - \sum_{m,n\in\mathcal{I}_N} \mathsf{L}_{-m}\mathsf{B}_m[\mathsf{A}^{-1}]_{mn}\mathsf{D}_n^{\mathsf{T}}\mathsf{L}_n. \tag{77}$$

The infinite-harmonic Schur complement defines the exact periodic effective operator. In numerical calculations, the reciprocal lattice is truncated to $|n| \leq N$, corresponding to $2N + 1$ retained Fourier harmonics including the mean harmonic[3].

This Schur-complement representation assumes that $\mathsf{A}(k, s)$ is invertible. At an isolated zero-mean corrector resonance, A becomes singular and $\widetilde{\mathsf{L}}$ may develop a pole. The effective operator is then understood by continuation or an appropriate limiting formulation.

Having identified $\widetilde{\mathsf{L}}$, we can remove the sources and obtain the effective bulk operator

$$\mathsf{K}(k,s)\mathsf{w}_0 = 0, \qquad \mathsf{K}(k,s) = \mathsf{D}_0^{\mathsf{T}}\widetilde{\mathsf{L}}(k,s)\mathsf{B}_0, \tag{78}$$

from which we obtain the dispersion relation satisfying

$$\det \mathsf{K}(k,s) = 0. \tag{79}$$

The frequency s and Bloch wavenumber k are therefore independent arguments of $\widetilde{\mathsf{L}}(k, s)$ and become related only after the source-free condition (78) is imposed.

[3]Since the laminate properties considered below are piecewise constant and therefore discontinuous at material interfaces, the Fourier approximation converges only algebraically with the cutoff N, rather than exponentially. We therefore assess the numerical results by explicit convergence with respect to the Fourier cutoff

Table 2. Material properties used in the numerical calculations. The first three rows define the thermoelastic laminates. The final row gives the properties of the lossless elastic host used in Sec. 6.4; thermal properties are not required for this medium.

Material	C [GPa]	ρ [kg m^{-3}]	κ [W m^{-1}K^{-1}]	c [J m^{-3}K^{-1}]	β [Pa K^{-1}]	c_h [m s^{-1}]	Z_0 [Pa s m^{-1}]
SiO_2	73.0	2200	1.38	1.65×10^6	3.7×10^4	–	–
Diamond	1050	3520	719	1.78×10^6	1.0×10^6	–	–
Cu	117.2	8910	391.1	3.43×10^6	1.983×10^6	–	–
Elastic host	297	3887	–	–	–	8.741×10^3	3.3981×10^7

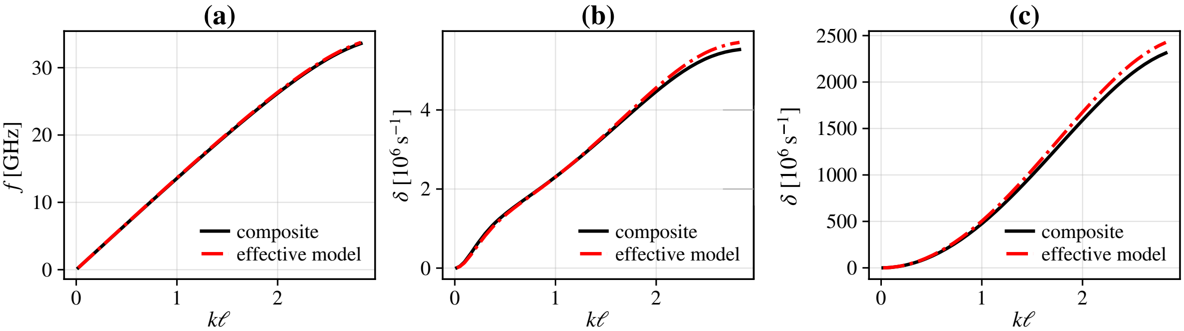

Fig. 2. Comparison between the exact Bloch spectrum of the 20-nm SiO_2|20-nm diamond|20-nm Cu laminate (composite, solid black) and the spectrum predicted by the effective model (red dash-dotted). The period is $\ell = 60$ nm and $\theta_R = 300$ K. (a) Oscillation frequency f of the acoustic-like branch. (b) Temporal decay rate $\delta = -\operatorname{Re} s$ of the acoustic-like branch. (c) Temporal decay rate of the thermal-like branch, whose oscillation frequency is negligible on the scale considered. The effective constitutive operator reproduces both the propagating acoustic-like and predominantly diffusive thermal-like dynamics of the heterogeneous laminate.

6. Numerical results

We next evaluate numerical examples, demonstrating the implications of our effective model. First, we validate its spectrum against the exact Bloch spectrum of the underlying heterogeneous laminate. We then use the effective description to identify how the emergent multiphysics couplings modify the attenuation of an acoustic-like mode. Next, we examine the symmetry and long-wavelength properties of these couplings by comparing asymmetric and centrosymmetric unit cells of identical composition. Finally, we demonstrate an observable consequence of the generalized thermoelastic impedance in a canonical scattering problem.

6.1. Validation against the exact Bloch spectrum

We first demonstrate that our effective bulk model reproduces the source-free spectrum of the underlying heterogeneous composite. We consider a laminate made of SiO_2|diamond|Cu. Each layer has a width of 20 nm, and their constituent properties are listed in Table 2. In our calculations, we use the reference temperature $\theta_R = 300$ K. The effective calculations in this subsection use the converged cutoff $N = 192$.

For a prescribed real Bloch wavenumber k, the effective spectrum is obtained from Eq. (79), with the nonlocal constitutive operator $\mathsf{L}(k, s)$ recomputed at each trial complex frequency s. The spectrum of the underlying laminate is calculated directly using the standard transfer matrix method, namely, propagating the exact state through the three homogeneous layers, together with the Bloch condition, as detailed in Appendix A. Figure 2 compares the resultant spectrum of the laminate (solid curves) with the spectrum of our effective model (dot-dashed curves) over $0.02 \lesssim k\ell \leq 0.9\pi$.

Panels (a)–(c) compare the acoustic oscillation frequency, the acoustic temporal decay rate, and the thermal-like decay rate, respectively. The curves shown correspond to the $N = 32$ Fourier truncation. At $k\ell = 1.2$, the relative discrepancies from the exact transfer-matrix result are 0.53% in acoustic frequency, 0.31% in acoustic decay, and 5.75% in thermal decay. Increasing the cutoff systematically reduces these discrepancies; at $N = 256$ they are 6.7×10^{-2}%, 1.9×10^{-2}%, and 6.8×10^{-1}%, respectively. The thermal-like branch converges more slowly because of its strongly diffusive character and the discontinuous laminate coefficients. The systematic decrease with increasing N confirms that the residual difference from the transfer-matrix spectrum is due to Fourier truncation rather than to an additional approximation in the homogenization theory. Thus, the infinite-harmonic effective operator reproduces both the propagating acoustic-like and predominantly diffusive thermal-like dynamics of the heterogeneous laminate.

6.2. Coupling-controlled acoustic attenuation

Having established the spectral correspondence, we next use the effective model to identify the constitutive couplings that determine the attenuation of an acoustic-like mode. We retain the same SiO_2, diamond, and Cu constituents and the same period

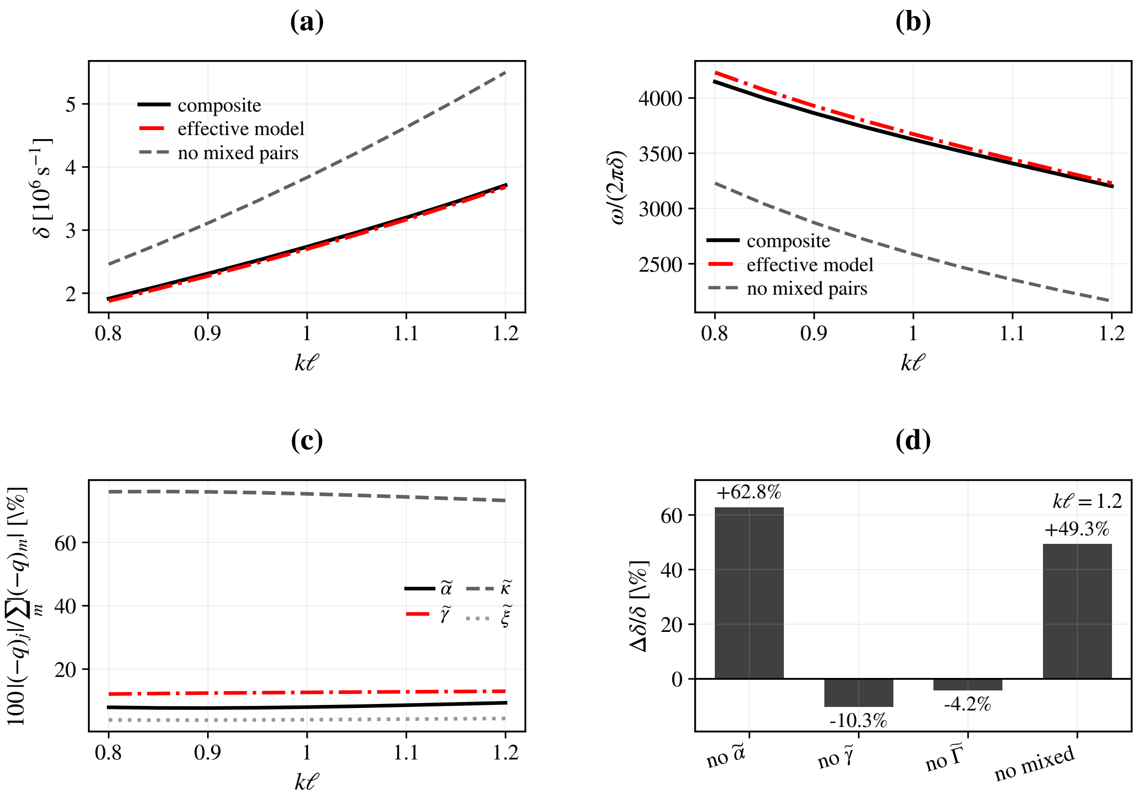

Fig. 3. Coupling-controlled attenuation of the acoustic-like mode in the 10.2-nm SiO_2|0.9-nm diamond|48.9-nm Cu laminate, with period $\ell = 60$ nm. (a) Temporal decay rate δ of the exact heterogeneous composite (solid black), the full effective model (red dash-dotted), and the diagnostic effective model obtained by removing all three mixed reciprocal pairs associated with $\widetilde{\alpha}$, $\widetilde{\gamma}$, and $\widetilde{\Gamma}$ (gray dashed). (b) The corresponding modal lifetime $\omega/(2\pi\delta)$, i.e., the number of oscillation cycles before an e^{-1} reduction in amplitude. (c) Normalized absolute contributions of $\widetilde{\alpha}$, $\widetilde{\gamma}$, $\widetilde{\kappa}$, and $\widetilde{\xi}$ to the constitutive heat flux, showing that thermal conduction remains the dominant irreversible mechanism while the mixed couplings make non-negligible contributions. (d) Relative change in δ at $k\ell = 1.2$ upon pair-preserving removal of $\widetilde{\alpha}$, $\widetilde{\gamma}$, or $\widetilde{\Gamma}$ individually, and upon removal of all three pairs. The ablations are diagnostic constitutive models rather than separately homogenized composites.

$\ell = 60$ nm, but consider different widths, namely, 10.2-nm SiO_2|0.9-nm diamond|48.9-nm Cu laminate. This laminate provides an attenuation-sensitive example in which the spectral influence of the emergent multiphysics couplings is substantially larger than in the equal-thickness reference cell.

To isolate the role of the mixed thermoelastic couplings, we perform pair-preserving constitutive ablations. The reciprocal pair associated with $\widetilde{\alpha}$, $\widetilde{\gamma}$, or $\widetilde{\Gamma}$ is set to zero, either individually or collectively, while every other entry of our effective constitutive operator is left unchanged. (These ablated operators are diagnostic models: they do not represent separately homogenized composites.) We then compare attenuation-related metrics of the resultant models with the exact model and the original composite.

Figure 3(a) compares the temporal decay rate of the exact heterogeneous acoustic branch (solid black) with the full effective model (dash-dot red) and with the diagnostic model in which all three mixed reciprocal pairs are removed (dash gray). At $k\ell = 1.2$, the full effective decay rate differs from the heterogeneous benchmark by less than 1%, whereas removal of all three mixed pairs increases the decay rate by approximately 50% relative to the full effective model. The same ablation barely changes the oscillation frequency, Thus, in this example, the mixed couplings modify the temporal attenuation far more strongly than the oscillation frequency.

Panel (b) expresses the same effect in terms of the modal lifetime $\omega/(2\pi\delta)$, which measures how many oscillation cycles a mode completes before its amplitude decays by a factor of e. At $k\ell = 1.2$, the full and no-mixed models give 3229 and no mixed = 2163, respectively, while the exact model gives 3202. Retaining the mixed pairs therefore increases the number of acoustic oscillations before an e^{-1} amplitude reduction by approximately 49%.

Panel (c) decomposes the heat flux into the normalized absolute contributions of $\widetilde{\kappa}$ and the emergent cross-couplings, showing that conduction remains the dominant irreversible mechanism, while the mixed couplings make non-negligible contributions. For example, at $k\ell = 1.2$, the normalized absolute contributions to the constitutive equation of the heat flux are 73% from $\widetilde{\kappa}$, while the mixed couplings $\widetilde{\gamma}, \widetilde{\alpha}, \widetilde{\xi}$ contribute $\simeq 13, 9$% and 4%, respectively. The mixed couplings should therefore not be interpreted as independent sources of dissipation. Rather, they modify the mechanical–thermal polarization of the acoustic-like eigenmode and

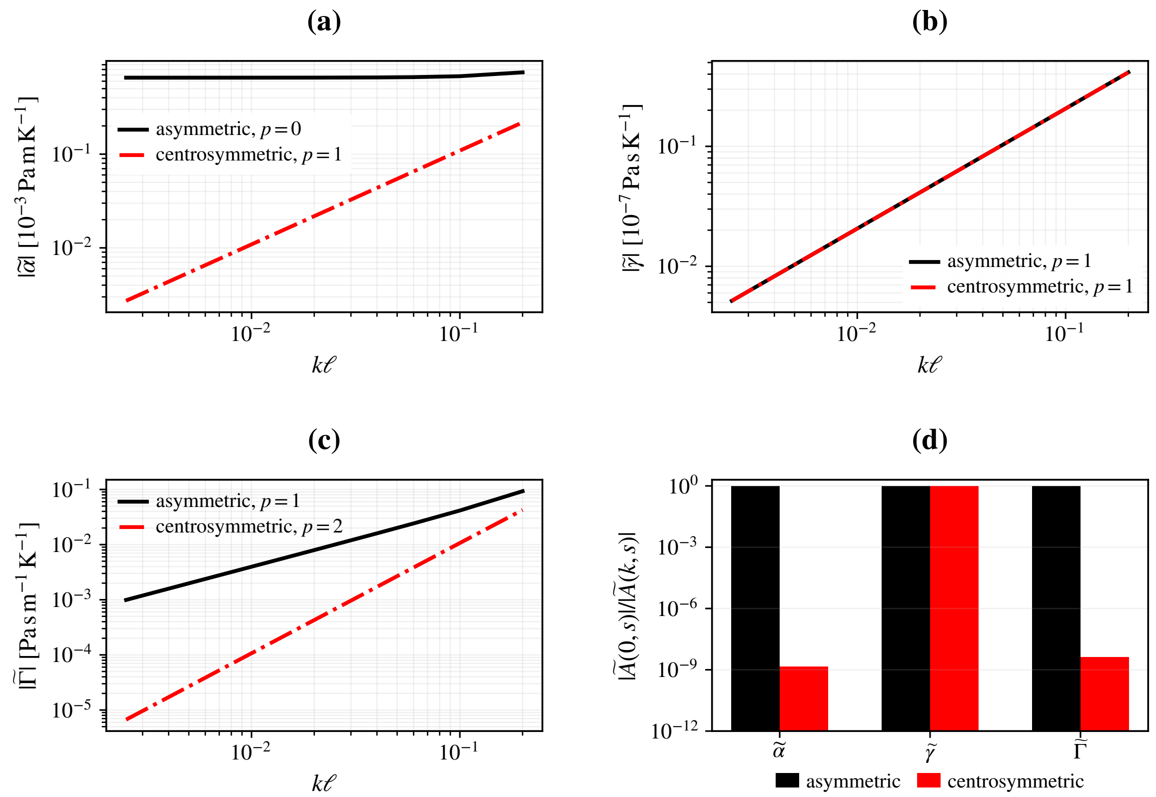

Fig. 4. Symmetry and long-wavelength behavior of the mixed thermoelastic cross-couplings along the acoustic branch. Panels (a)–(c) show $|\widetilde{\alpha}|$, $|\widetilde{\gamma}|$, and $|\widetilde{\Gamma}|$ for both the asymmetric laminate and its same-composition centrosymmetric control. Centrosymmetry changes the leading scalings of the inversion-odd couplings from $|\widetilde{\alpha}| \sim (k\ell)^0$ to $(k\ell)^1$ and from $|\widetilde{\Gamma}| \sim (k\ell)^1$ to $(k\ell)^2$, while the inversion-even $\widetilde{\gamma}$ retains the $(k\ell)^1$ scaling. Panel (d) shows the spatially local fraction $|\widetilde{A}(0,s)|/|\widetilde{A}(k,s)|$, demonstrating that centrosymmetry suppresses the local parts of $\widetilde{\alpha}$ and $\widetilde{\Gamma}$, whereas $\widetilde{\gamma}$ remains locally allowed.

thereby regulate how strongly it accesses the diffusive thermal sector.

Panel (d) further separates these effects, by showing a bar chart of the change in the acoustic decay, $\Delta\delta/\delta$, at representative wavenumber $k\ell = 1.2$, when removing the mixed couplings individually or collectively, thereby identifying their distinct influences on attenuation. Thus, removal of the $\widetilde{\alpha}$ pair increases δ by 62.76%, whereas removal of the $\widetilde{\gamma}$ and $\widetilde{\Gamma}$ pairs changes it by −10.27% and −4.19%, respectively. Removing all three pairs simultaneously produces the net 49.29% change reported above. These changes are not additive because each ablation modifies the complete coupled eigenproblem and therefore changes both its eigenvalue and eigenvector. In this laminate, $\widetilde{\alpha}$ is the dominant attenuation-reducing mixed coupling, while $\widetilde{\gamma}$ and $\widetilde{\Gamma}$ partially oppose its effect.

6.3. Symmetry origin of the mixed cross-couplings

The preceding numerical examples demonstrate that the mixed couplings $\widetilde{\alpha}$, $\widetilde{\gamma}$, and $\widetilde{\Gamma}$ can have significant spectral consequences. We now use the effective operator to test the inversion and long-wavelength classifications derived in Sec. 5.1. To this end, we compare the asymmetric cell introduced above with a same-composition centrosymmetric control, obtained by symmetrizing the unit cell while preserving its period and constituent volume fractions.

Figures 4(a)–(c) show the magnitudes of $\widetilde{\alpha}$, $\widetilde{\gamma}$, and $\widetilde{\Gamma}$, respectively, along the acoustic branch. For the asymmetric cell, we obtain $|\widetilde{\alpha}| \sim (k\ell)^0$, $|\widetilde{\gamma}| \sim (k\ell)^1$, and $|\widetilde{\Gamma}| \sim (k\ell)^1$. In the centrosymmetric control, the corresponding scalings are $|\widetilde{\alpha}| \sim (k\ell)^1$, $|\widetilde{\gamma}| \sim (k\ell)^1$, and $|\widetilde{\Gamma}| \sim (k\ell)^2$. Thus, centrosymmetry changes the leading long-wavelength order of the inversion-odd couplings $\widetilde{\alpha}$ and $\widetilde{\Gamma}$, while leaving that of the inversion-even $\widetilde{\gamma}$ unchanged. We note that, since s is complex and the thermal sector is dissipative, $\mathrm{Re}\,\widetilde{A}$ and $\mathrm{Im}\,\widetilde{A}$, where $\widetilde{A} = \widetilde{\alpha}, \widetilde{\gamma}, \widetilde{\Gamma}$, do not provide universal symmetry labels; the relevant classification is instead the inversion parity of the $k = 0$ contribution.

These scalings follow directly from combining inversion parity with the low-frequency orders derived in Sec. 5.1. The inversion-odd coupling $\widetilde{\alpha} = O(1)$ may possess a finite spatially local value when centrosymmetry is broken. In the centrosymmetric cell, however, $\widetilde{\alpha}(0,s) = 0$, so that its leading contribution is the odd-in-k nonlocal term and $\widetilde{\alpha} = O(k)$. The inversion-even coupling $\widetilde{\gamma} = O(s)$ is locally allowed in both geometries; since $s = O(k)$ along the acoustic branch, this gives $\widetilde{\gamma} = O(k)$ in either case. Finally, $\widetilde{\Gamma} = O(s)$ is inversion odd. Broken centrosymmetry permits a local contribution, giving $\widetilde{\Gamma} = O(s) = O(k)$, whereas centrosymmetry removes this contribution and introduces an additional odd-in-k factor, so that $\widetilde{\Gamma} = O(sk) = O(k^2)$.

Panel (d) tests the same interpretation directly, without relying on the fitted exponents, by showing the spatially local fraction $|\widetilde{A}(0,s)|/|\widetilde{A}(k,s)|$. A value close to unity indicates that the coupling at the considered (k,s) is dominated by its $k=0$ constitutive contribution, whereas a value close to zero indicates that it arises predominantly from finite-k spatial dispersion. In the asymmetric laminate, all three couplings are essentially spatially local in the long-wavelength regime. In the centrosymmetric control, by contrast, the local contributions to the inversion-odd $\widetilde{\alpha}$ and $\widetilde{\Gamma}$ are suppressed, so that their remaining finite-k values are nonlocal, whereas $\widetilde{\gamma}$ remains predominantly local because its even inversion character does not forbid $\widetilde{\gamma}(0,s)$.

Figure 4 therefore distinguishes two origins of effective thermoelastic cross-coupling. Broken microscopic centrosymmetry permits spatially local bianisotropic couplings that are forbidden in the centrosymmetric material, while finite-wavenumber spatial dispersion can generate residual inversion-odd couplings even when the local contribution vanishes. This distinction provides a direct thermoelastic analogue of the separation between symmetry-induced local bianisotropy and nonlocal coupling in wave metamaterials.

6.4. Observable signature of the generalized thermoelastic impedance

Finally, we demonstrate an observable consequence of the off-diagonal thermoelastic impedance using a canonical scattering problem. Specifically, we consider a lossless elastic half-space occupying $x < 0$ (specific properties listed in Table 2), perfectly bonded to our effective medium occupying $x > 0$, obtained from the homogenization of a unit cell with the same Cu|SiO_2|diamond constituents as before, now with the widths 8, 10.4 amd 61.6 nm, respectively[4]. The effective medium is driven by a monochromatic mechanical wave of angular frequency ω incident from the elastic half-space. At the interface, we consider the adiabatic boundary condition $q(0) = 0$, so that no heat flux is supplied through the interface and any nonzero surface-temperature response is generated by mechanical-to-thermal conversion in the effective medium.

In terms of the modal boundary map Z^+ (57), with components Z^+_{ij}, we obtain

$$\frac{\theta(0)}{u(0)} = -\frac{Z^+_{21}}{Z^+_{22}}, \tag{80}$$

while elimination of the thermal boundary variable gives the mechanical input impedance

$$Z_{\text{in}} = \frac{1}{\mathrm{i}\omega}\left(Z^+_{11} - \frac{Z^+_{12}Z^+_{21}}{Z^+_{22}}\right). \tag{81}$$

Thus, even when ordinary mechanical reflection is very small, the off-diagonal boundary response can generate a finite oscillatory surface temperature. We characterize this cross-channel conversion by

$$\Theta = \frac{\theta(0)}{\theta_R \epsilon_i}, \tag{82}$$

where ϵ_i is the incident strain amplitude in the elastic host.

In the following calculation, we consider the frequency $\omega_* = 2.35 \times 10^8\,\text{rad s}^{-1}$. With the present $e^{\mathrm{i}\omega t}$ convention, the incident elastic wave travelling from the host toward the interface has $\sigma_i/v_i = -Z_0$. Consequently, $r = (Z_0 + Z_{\text{in}})/(Z_0 - Z_{\text{in}})$, and ordinary mechanical reflection is suppressed when $Z_{\text{in}} \simeq -Z_0$. At ω_* this condition is nearly satisfied, giving $|r| \simeq 3.25 \times 10^{-5}$ and thereby isolating the mechanically generated thermal response.

Figure 5 summarizes the orientation-sensitive mechanical-to-thermal conversion predicted by the effective medium and identifies its constitutive origin. Panel (a) shows the magnitude of the normalized surface-temperature response, $|\Theta|$, for the asymmetric cell (black curves) and its physical mirror (red curves), as function of ω. The full effective model is compared with the diagnostic model (dot-dash curves) in which the three mixed reciprocal pairs associated with $\widetilde{\alpha}$, $\widetilde{\gamma}$, and $\widetilde{\Gamma}$ are removed. Throughout the plotted frequency range, the ordinary mechanical reflection remains below 6×10^{-5}; hence, the relevant observable is the cross-channel thermal response rather than the same-channel reflection coefficient. At ω_*, the full model gives $|\Theta_{\rightarrow}| = 0.4139$ and $|\Theta_{\leftarrow}| = 0.3536$, where the subscripts $\rightarrow$ and $\leftarrow$ denote the cell and its mirror, respectively. For an incident strain amplitude $|\epsilon_i| = 10^{-4}$ and reference temperature $\theta_R = 300\,\text{K}$, these values correspond to surface-temperature amplitudes of approximately 12.42 mK and 10.61 mK.

Panel (b) shows the corresponding orientation-dependent phase splitting, defined by

$$\Delta\phi_\Theta = \left|\arg\left(\frac{\Theta_{\rightarrow}}{\Theta_{\leftarrow}}\right)\right|, \tag{83}$$

where the phase is taken modulo 2π and represented by the smallest angular separation. At ω_*, the phases of the cell and its mirror responses are approximately $-176.15°$ and $174.89°$, respectively, giving $\Delta\phi_\Theta \simeq 8.96°$. The full effective model therefore predicts an orientation dependence in both the magnitude and phase of the mechanically generated thermal response. Removing the mixed reciprocal pairs strongly suppresses both signatures.

[4]The cell was selected by a search for a large orientation-sensitive mechanical-to-thermal conversion response in a regime where the spatially local reduction remains quantitatively controlled.

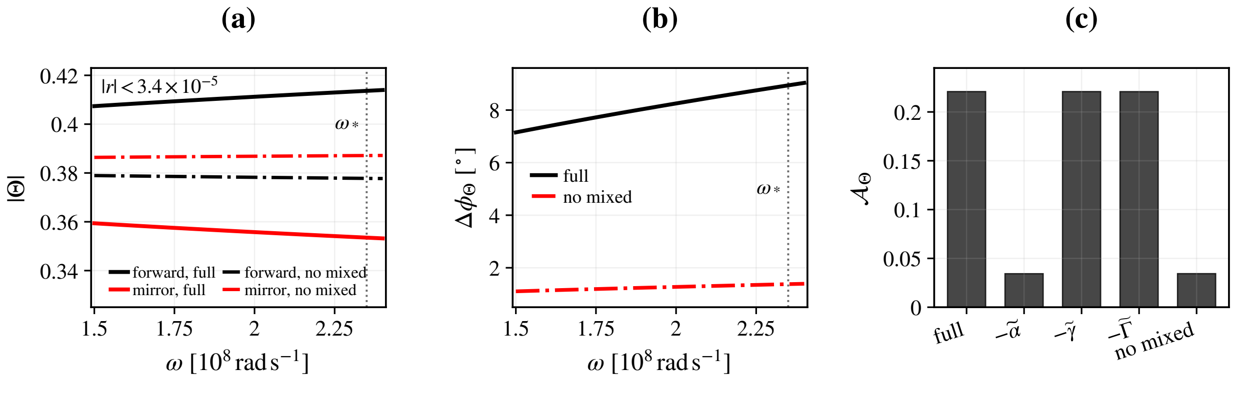

Fig. 5. Orientation-sensitive mechanical-to-thermal conversion at an elastic/effective-thermoelastic interface. (a) Magnitude of the normalized surface-temperature response, $|\Theta|$, for the asymmetric unit cell (black) and its physical mirror (red), comparing the full effective model (solid) with the diagnostic model (dot-dashed) in which the three mixed reciprocal pairs associated with $\widetilde{\alpha}$, $\widetilde{\gamma}$, and $\widetilde{\Gamma}$ are removed. The vertical marker denotes $\omega_* = 2.35 \times 10^8\,\mathrm{rad\,s^{-1}}$, where ordinary mechanical reflection is nearly suppressed. (b) Corresponding orientation-dependent phase splitting $\Delta\phi_\Theta$. (c) Complex asymmetry measure $\mathcal{A}_\Theta$ at ω_* for the full model and for pair-preserving constitutive ablations. Removing $\widetilde{\alpha}$ nearly reproduces the suppression obtained by removing all three mixed pairs, whereas removing $\widetilde{\gamma}$ or $\widetilde{\Gamma}$ has little effect, identifying the inversion-odd $\widetilde{\alpha}$ coupling as the dominant term capturing directional thermomechanical conversion.

Panel (c) isolates the constitutive origin of this orientation dependence at ω_*. We quantify the difference between the forward and mirrored responses using the normalization-independent complex asymmetry measure

$$\mathcal{A}_\Theta = \frac{2|\Theta_\rightarrow - \Theta_\leftarrow|}{|\Theta_\rightarrow| + |\Theta_\leftarrow|}. \tag{84}$$

For the full effective medium, $\mathcal{A}_\Theta = 0.2211$, whereas removing all three mixed pairs reduces this value to $\mathcal{A}_\Theta = 0.03434$. Removing $\widetilde{\alpha}$ alone gives $\mathcal{A}_\Theta = 0.03428$, essentially reproducing the collapse obtained when all three mixed pairs are removed, while suppressing either $\widetilde{\gamma}$ or $\widetilde{\Gamma}$ leaves the full result nearly unchanged. The orientation-sensitive impedance response in this nonresonant example is therefore controlled predominantly by the inversion-odd $\widetilde{\alpha}$ pair. It should accordingly be interpreted as an observable $\widetilde{\alpha}$-dominated bianisotropic conversion effect, rather than as a comparable manifestation of all three mixed thermoelastic couplings.

Finally, we note that this observable lies within the spatially local regime of the effective description. At ω_*, the normalized elastic and thermal wavenumbers are $|k_a\ell| = 2.15 \times 10^{-3}$ and $|k_t\ell| = 0.527$, respectively. Furthermore, the relative errors between the local effective and finite-wavenumber acoustic and thermal roots are 2.35×10^{-5} and 1.36×10^{-3}, respectively, while the corresponding finite-k constitutive deviations are 1.18×10^{-5} and 2.94×10^{-3}.

7. Summary and discussion

We have developed an exact source-driven homogenization framework for heterogeneous thermoelastic media, extending Willis-type dynamic homogenization to systems in which propagating elastic waves coexist with thermal diffusion. The formulation is based on a Green-function representation and ensemble averaging and yields nonlocal constitutive relations between the macroscopic stress, momentum, heat flux, and entropy and the corresponding strain, velocity, temperature gradient, and temperature. For periodic media, we have recast the general formulation in Fourier space, where elimination of the nonzero microscopic harmonics through a Schur complement provides the effective constitutive operator as a function of independently prescribed wavenumber and frequency.

The resultant effective description is considerably richer than standard thermoelasticity. In addition to the conventional elastic, inertial, conductive, caloric, and thermoelastic terms, it contains the Willis and thermal-bianisotropic pairs and three reciprocal mixed pairs, $\widetilde{\boldsymbol{\alpha}}$, $\widetilde{\boldsymbol{\gamma}}$, and $\widetilde{\boldsymbol{\Gamma}}$, which couple the propagating and diffusive sectors. We have shown that their spatial symmetry distinguishes two origins of effective cross-coupling. Broken centrosymmetry permits spatially local inversion-odd couplings, whereas finite-wavenumber spatial dispersion can retain such couplings even when centrosymmetry eliminates their local part. In the spatially local bulk equations, $\widetilde{\boldsymbol{\alpha}}$ generates curvature–gradient conversion, $\widetilde{\boldsymbol{\gamma}}$ modifies the rate-dependent thermoelastic interaction, and $\widetilde{\boldsymbol{\Gamma}}$ introduces a zero-order thermomechanical coupling. By contrast, the Willis and thermal-bianisotropic pairs cancel from the local source-free bulk equations but remain present in the boundary response.

We tested these predictions using one-dimensional thermoelastic laminates. First, the source-driven effective model reproduces both the propagating acoustic-like and predominantly diffusive thermal-like branches of the exact heterogeneous Bloch spectrum. Second, pair-preserving constitutive ablations show that the mixed couplings can significantly affect acoustic attenuation while producing only a small change in oscillation frequency. In the attenuation-sensitive example considered, removing all three mixed pairs changes the acoustic decay rate by approximately 50%. The individual contributions are competing and nonadditive: the mixed couplings do not act as independent sources of dissipation, but modify the mechanical–thermal polarization of the mode and thereby regulate its access to the dissipative thermal sector. Third, comparison between an asymmetric laminate and a same-composition centrosymmetric control confirms the predicted inversion classification and separates local symmetry-induced bianisotropy from residual finite-wavenumber nonlocal coupling.

Finally, we connected the bulk constitutive theory to a measurable boundary response by introducing a generalized thermoelastic modal impedance. In a canonical scattering problem between a homogeneous elastic half-space and a semi-infinite effective thermoelastic medium, a purely elastic incident wave generates a finite surface-temperature response even when ordinary mechanical reflection is nearly suppressed. Reversal of the asymmetric microstructure changes both the magnitude and phase of this response. Constitutive ablations show that, in the example studied here, this directional thermomechanical conversion is controlled predominantly by the inversion-odd stress–temperature-gradient coupling $\widetilde{\boldsymbol{\alpha}}$. The result provides a direct observable signature of a coupling that is otherwise embedded in the full nonlocal constitutive operator.

Collectively, these results show that homogenization of coupled wave–diffusion media does more than renormalize conventional material parameters: it can generate constitutive channels that control bulk attenuation, modal polarization, and boundary impedance. The mechanism identified here is not specific to thermoelasticity, but follows from the coexistence of interacting propagating and diffusive fields. We therefore expect analogous multiphysics bianisotropy to arise in other heterogeneous wave–diffusion systems. More generally, the present framework provides a route for separating the roles of microscopic symmetry and spatial nonlocality, and for identifying macroscopic phenomena that are obscured in the detailed heterogeneous description.

Acknowledgments

GS acknowledges funding by the European Union (ERC, EXCEPTIONAL, Project No. 101045494). Funded by the European Union. Views and opinions expressed are, however, those of the authors only and do not necessarily reflect those of the European Union or the European Research Council Executive Agency. Neither the European Union nor the granting authority can be held responsible for them. GS was also sponsored by the Army Research Office and was accomplished under Grant Number W911NF-26-1-A161. The views and conclusions contained in this document are those of the authors and should not be interpreted as representing the official policies, either expressed or implied, of the Army Research Office or the U. S. Government. The U.S. Government is authorized to reproduce and distribute reprints for Government purposes notwithstanding any copyright notation herein.

Appendix A. Modal solutions and the transfer matrix method

This appendix details the exact layered-medium calculation used to obtain the heterogeneous Bloch spectrum in Sec. 6.1. Consider a one-dimensional laminate composed of homogeneous thermoelastic layers $r = 1, \ldots, R$. Layer r occupies $x_{r-1} < x < x_r$, has thickness $d_r = x_r - x_{r-1}$, and is characterized by the scalar properties C_r, ρ_r, κ_r, c_r, and β_r. The period is

$$\ell = \sum_{r=1}^{R} d_r. \tag{A1}$$

The constituents used in the numerical examples are reciprocal, so that the one-dimensional specialization of Eq. (1) is

$$\sigma = C_r u_{,x} - \beta_r \theta, \qquad p = \rho_r s u, \qquad -q = \kappa_r \theta_{,x}, \qquad \theta_R \eta = \theta_R \beta_r u_{,x} + c_r \theta. \tag{A2}$$

In the absence of body-force and heat sources, the balance equations reduce to

$$\sigma_{,x} - sp = 0, \qquad (-q)_{,x} - s\theta_R \eta = 0. \tag{A3}$$

Introduce the state vector

$$\mathsf{y} = \begin{pmatrix} \sigma \\ u \\ -q \\ \theta \end{pmatrix}. \tag{A4}$$

Using Eqs. (A2) and (A3), the fields in layer r satisfy the constant-coefficient first-order system

$$\mathsf{y}_{,x} = \mathsf{M}_r(s)\mathsf{y}, \tag{A5}$$

where

$$\mathsf{M}_r(s) = \begin{pmatrix} 0 & \rho_r s^2 & 0 & 0 \\ C_r^{-1} & 0 & 0 & \beta_r/C_r \\ s\theta_R\beta_r/C_r & 0 & 0 & s(c_r + \theta_R\beta_r^2/C_r) \\ 0 & 0 & \kappa_r^{-1} & 0 \end{pmatrix}. \tag{A6}$$

Thus, a modal solution may be written as

$$\mathsf{y}(x) = \widehat{\mathsf{y}}\, e^{\lambda(x-x_{r-1})}, \qquad (\mathsf{M}_r - \lambda \mathsf{I})\,\widehat{\mathsf{y}} = \mathsf{0}. \tag{A7}$$

The same spatial exponent follows directly from the displacement–temperature form of the field equations. Taking

$$u(x) = \widehat{u}\, e^{\lambda x}, \qquad \theta(x) = \widehat{\theta}\, e^{\lambda x}, \tag{A8}$$

gives

$$\begin{pmatrix} C_r\lambda^2 - \rho_r s^2 & -\beta_r \lambda \\ -\theta_R \beta_r s\lambda & \kappa_r\lambda^2 - c_r s \end{pmatrix} \begin{pmatrix} \widehat{u} \\ \widehat{\theta} \end{pmatrix} = \mathsf{0}. \tag{A9}$$

Accordingly, the four spatial exponents are the roots of

$$\left(C_r\lambda^2 - \rho_r s^2\right)\left(\kappa_r\lambda^2 - c_r s\right) - \theta_R\beta_r^2 s\lambda^2 = 0. \tag{A10}$$

This equation is quadratic in λ^2. Defining

$$a_r(s) := C_r c_r s + \rho_r\kappa_r s^2 + \theta_R\beta_r^2 s, \tag{A11}$$

the two values of λ^2 are

$$\mu_{r,\pm}(s) = \frac{a_r(s) \pm \sqrt{a_r^2(s) - 4C_r\kappa_r\rho_r c_r s^3}}{2C_r\kappa_r}. \tag{A12}$$

Hence the four layer modes can be ordered as

$$\lambda_{r1} = +\sqrt{\mu_{r,+}}, \qquad \lambda_{r2} = -\sqrt{\mu_{r,+}}, \qquad \lambda_{r3} = +\sqrt{\mu_{r,-}}, \qquad \lambda_{r4} = -\sqrt{\mu_{r,-}}. \tag{A13}$$

The association of the two pairs with the acoustic-like and thermal-like modes is most transparent in the uncoupled limit $\beta_r \to 0$, for which Eq. (A10) factorizes and gives

$$\lambda^{\pm}_{m,r} = \pm s\sqrt{\frac{\rho_r}{C_r}}, \qquad \lambda^{\pm}_{t,r} = \pm\sqrt{\frac{c_r s}{\kappa_r}}. \tag{A14}$$

For $s = \mathrm{i}\omega$, the first pair describes propagating elastic waves, whereas the second pair describes thermal diffusion. Away from $\beta_r = 0$, the two families hybridize but may be followed continuously from these limits.

For $\beta_r\lambda_{rj} \neq 0$, define the modal temperature–displacement polarization

$$\chi_{rj} := \frac{\widehat{\theta}_{rj}}{\widehat{u}_{rj}} = \frac{C_r\lambda_{rj}^2 - \rho_r s^2}{\beta_r\lambda_{rj}} = \frac{\theta_R\beta_r s\lambda_{rj}}{\kappa_r\lambda_{rj}^2 - c_r s}. \tag{A15}$$

Choosing $\widehat{u}_{rj} = 1$, a corresponding state eigenvector is

$$\widehat{\mathsf{y}}_{rj} = \begin{pmatrix} C_r\lambda_{rj} - \beta_r\chi_{rj} \\ 1 \\ \kappa_r\lambda_{rj}\chi_{rj} \\ \chi_{rj} \end{pmatrix}. \tag{A16}$$

The first component may equivalently be written as $\rho_r s^2/\lambda_{rj}$ by virtue of Eq. (A10). When $\beta_r = 0$, the decoupled eigenvectors can instead be taken directly as

$$\widehat{\mathsf{y}}^{\pm}_{m,r} = \begin{pmatrix} C_r\lambda^{\pm}_{m,r} \\ 1 \\ 0 \\ 0 \end{pmatrix}, \qquad \widehat{\mathsf{y}}^{\pm}_{t,r} = \begin{pmatrix} 0 \\ 0 \\ \kappa_r\lambda^{\pm}_{t,r} \\ 1 \end{pmatrix}. \tag{A17}$$

Collecting the four eigenvectors into the modal matrix

$$\mathsf{Q}_r = \begin{pmatrix} | & | & | & | \\ \widehat{\mathsf{y}}_{r1} & \widehat{\mathsf{y}}_{r2} & \widehat{\mathsf{y}}_{r3} & \widehat{\mathsf{y}}_{r4} \\ | & | & | & | \end{pmatrix}, \tag{A18}$$

the complete field in layer r can be written as

$$\mathsf{y}(x) = \mathsf{Q}_r \begin{pmatrix} e^{\lambda_{r1}(x-x_{r-1})} & 0 & 0 & 0 \\ 0 & e^{\lambda_{r2}(x-x_{r-1})} & 0 & 0 \\ 0 & 0 & e^{\lambda_{r3}(x-x_{r-1})} & 0 \\ 0 & 0 & 0 & e^{\lambda_{r4}(x-x_{r-1})} \end{pmatrix} \mathsf{a}_r, \tag{A19}$$

where a_r is the four-component vector of modal amplitudes.

At a perfectly bonded interface, displacement, temperature, normal stress, and heat flux are continuous. The state (A4) is therefore continuous across every internal interface. Propagation across layer r gives

$$\mathsf{y}(x_r) = \mathsf{T}_r(s)\,\mathsf{y}(x_{r-1}), \tag{A20}$$

with the exact layer transfer matrix

$$\mathsf{T}_r(s) = \mathsf{Q}_r\mathsf{E}_r(d_r)\mathsf{Q}_r^{-1} = e^{\mathsf{M}_r(s)d_r}, \tag{A21}$$

where

$$\mathsf{E}_r(d_r) = \operatorname{diag}\left(e^{\lambda_{r1}d_r}, e^{\lambda_{r2}d_r}, e^{\lambda_{r3}d_r}, e^{\lambda_{r4}d_r}\right). \tag{A22}$$

The two expressions in Eq. (A21) are identical. The modal form makes the acoustic–thermal content explicit, whereas the matrix exponential provides a convenient implementation that does not depend on a particular normalization or ordering of the eigenvectors and remains well defined at modal degeneracies.

For a unit cell whose layers are ordered from left to right as $1, 2, \ldots, R$, repeated application of Eq. (A20) gives

$$\mathsf{y}(x_0+\ell) = \mathsf{T}_{\mathrm{cell}}(s)\mathsf{y}(x_0), \qquad \mathsf{T}_{\mathrm{cell}}(s) = \mathsf{T}_R(s)\mathsf{T}_{R-1}(s)\cdots\mathsf{T}_1(s). \tag{A23}$$

Because each constituent layer is homogeneous, no spatial discretization is introduced in this calculation: each T_r is the exact propagator of the corresponding constant-coefficient thermoelastic equations.

For an infinite periodic laminate, the Bloch condition in the convention used throughout the manuscript is

$$\mathsf{y}(x+\ell) = e^{\mathrm{i}k\ell}\,\mathsf{y}(x). \tag{A24}$$

Combining Eqs. (A23) and (A24) gives the unit-cell eigenproblem

$$\left[\mathsf{T}_{\mathrm{cell}}(s) - e^{\mathrm{i}k\ell}\mathsf{I}\right]\mathsf{y}(x_0) = \mathsf{0}. \tag{A25}$$

A nontrivial Bloch mode therefore exists if and only if

$$\det\left[\mathsf{T}_{\mathrm{cell}}(s) - e^{\mathrm{i}k\ell}\mathsf{I}\right] = 0, \tag{A26}$$

which is the transfer-matrix condition used for the heterogeneous benchmark in the examples of Sec. 6. These calculations prescribed k as a real Bloch wavenumber and Eq. (A26) is solved for the generally complex Laplace frequency s. The acoustic-like branch is identified by its continuation from the elastic pair (A14), while the thermal-like branch is identified by its continuation from the diffusive pair. The transfer-matrix spectrum thus contains the coupled elastic and thermal dynamics of the actual piecewise-homogeneous laminate and serves as a benchmark for the source-driven effective dispersion relation.

References

Bensoussan, A., Lions, J.L., Papanicolaou, G., 2011. Asymptotic analysis for periodic structures. volume 374. American Mathematical Soc.

Biot, M.A., 1956. Thermoelasticity and irreversible thermodynamics. J. Appl. Phys. 27, 240–253. URL: https://doi.org/10.1063/1.1722351, doi:10.1063/1.1722351, arXiv:https://pubs.aip.org/aip/jap/article-pdf/27/3/240/7922890/240_1_online.pdf.

Brenner, T.M., Gehrmann, C., Korobko, R., Livneh, T., Egger, D.A., Yaffe, O., 2020. Anharmonic host-lattice dynamics enable fast ion conduction in superionic AgI. Phys. Rev. Materials 4, 115402. doi:10.1103/PhysRevMaterials.4.115402.

Fietz, C., Shvets, G., 2010. Current-driven metamaterial homogenization. Physica B 405, 2930–2934. doi:10.1016/j.physb.2010.01.006.

Hussein, M.I., Leamy, M.J., Ruzzene, M., 2014. Dynamics of Phononic Materials and Structures: Historical Origins, Recent Progress, and Future Outlook. Appl. Mech. Rev. 66, 40802. URL: http://dx.doi.org/10.1115/1.4026911.

Hutson, A.R., White, D.L., 1962. Elastic wave propagation in piezoelectric semiconductors. J. Appl. Phys. 33, 40–47. doi:10.1063/1.1728525.

Kadic, M., Bückmann, T., Schittny, R., Wegener, M., 2013. Metamaterials beyond electromagnetism. Rep. Prog. Phys. 76, 126501. URL: http://stacks.iop.org/0034-4885/76/i=12/a=126501.

Kadic, M., Milton, G.W., van Hecke, M., Wegener, M., 2019. 3d metamaterials. Nat. Rev. Phys. 1, 198–210. URL: https://doi.org/10.1038/s42254-018-0018-y, doi:10.1038/s42254-018-0018-y.

Li, Y., Li, W., Han, T., Zheng, X., Li, J., Li, B., Fan, S., Qiu, C.W., 2021. Transforming heat transfer with thermal metamaterials and devices. Nat. Rev. Mater. 6, 488–507. URL: https://doi.org/10.1038/s41578-021-00283-2, doi:10.1038/s41578-021-00283-2.

Liu, Y., Liang, Z., Zhu, J., Xia, L., Mondain-Monval, O., Brunet, T., Alù, A., Li, J., 2019. Willis metamaterial on a structured beam. Phys. Rev. X 9, 011040. doi:10.1103/PhysRevX.9.011040.

Melnikov, A., Chiang, Y.K., Quan, L., Oberst, S., Alù, A., Marburg, S., Powell, D., 2019. Acoustic meta-atom with experimentally verified maximum Willis coupling. Nat. Commun. 10, 3148. URL: https://doi.org/10.1038/s41467-019-10915-5, doi:10.1038/s41467-019-10915-5.

Meng, S., Guzina, B.B., 2018. On the dynamic homogenization of periodic media: Willis' approach versus two-scale paradigm. Proc. R. Soc. A 474. URL: http://rspa.royalsocietypublishing.org/content/474/2213/20170638, doi:10.1098/rspa.2017.0638.

Milton, G.W., . A unifying perspective on linear continuum equations prevalent in science. part II: Canonical forms for time-harmonic equations. arXiv:2006.02433.

Milton, G.W., 2002. The Theory of Composites. volume 6 of *Cambridge Monographs on Applied and Computational Mathematics*. Cambridge University Press, Cambridge. doi:10.1017/CBO9780511613357.

Milton, G.W., 2007. New metamaterials with macroscopic behavior outside that of continuum elastodynamics. New J. Phys. 9, 359–359. URL: https://doi.org/10.1088%2F1367-2630%2F9%2F10%2F359, doi:10.1088/1367-2630/9/10/359.

Milton, G.W., Briane, M., Willis, J.R., 2006. On cloaking for elasticity and physical equations with a transformation invariant form. New J. Phys. 8, 248. URL: http://stacks.iop.org/1367-2630/8/i=10/a=248.

Muhafra, A., Kosta, M., Torrent, D., Pernas-Salomón, R., Shmuel, G., 2022. Homogenization of piezoelectric planar Willis materials undergoing antiplane shear. Wave Motion 108, 102833. doi:10.1016/j.wavemoti.2021.102833.

Muhafra, K., Haberman, M.R., Shmuel, G., 2023. Discrete one-dimensional models for the electromomentum coupling. Phys. Rev. Applied 20, 014042. doi:10.1103/PhysRevApplied.20.014042.

Muhlestein, M.B., Sieck, C.F., Wilson, P.S., Haberman, M.R., 2017. Experimental evidence of Willis coupling in a one-dimensional effective material element. Nat. Commun. 8, 15625. doi:10.1038/ncomms15625.

Nassar, H., He, Q.C., Auffray, N., 2015. Willis elastodynamic homogenization theory revisited for periodic media. J. Mech. Phys. Solids 77, 158–178. URL: https://www.sciencedirect.com/science/article/pii/S0022509614002579, doi:10.1016/j.jmps.2014.12.011.

Nassar, H., He, Q.C., Auffray, N., 2016. On asymptotic elastodynamic homogenization approaches for periodic media. J. Mech. Phys. Solids 88, 274–290. URL: http://www.sciencedirect.com/science/article/pii/S0022509615303859, doi:10.1016/j.jmps.2015.12.020.

Norris, A.N., Shuvalov, A.L., Kutsenko, A.A., 2012. Analytical formulation of three-dimensional dynamic homogenization for periodic elastic systems. Proc. R. Soc. A URL: http://rspa.royalsocietypublishing.org/content/early/2012/02/14/rspa.2011.0698, doi:10.1098/rspa.2011.0698.

Peng, Y.G., Mazor, Y., Alù, A., 2022. Fundamentals of acoustic willis media. Wave Motion 112, 102930. doi:10.1016/j.wavemoti.2022.102930.

Pernas-Salomón, R., Haberman, M.R., Norris, A.N., Shmuel, G., 2021. The electromomentum effect in piezoelectric Willis scatterers. Wave Motion 106, 102797. doi:10.1016/j.wavemoti.2021.102797.

Pernas-Salomón, R., Shmuel, G., 2018. Dynamic homogenization of composite and locally resonant flexural systems. J. Mech. Phys. Solids 119, 43–59. URL: http://www.sciencedirect.com/science/article/pii/S0022509618302503, doi:10.1016/j.jmps.2018.06.011.

Pernas-Salomón, R., Shmuel, G., 2020a. Fundamental principles for generalized Willis metamaterials. Phys. Rev. Applied 14, 064005. doi:10.1103/PhysRevApplied.14.064005.

Pernas-Salomón, R., Shmuel, G., 2020b. Symmetry breaking creates electro-momentum coupling in piezoelectric metamaterials. J. Mech. Phys. Solids 134, 103770. doi:10.1016/j.jmps.2019.103770.

Ponge, M.F., Poncelet, O., Torrent, D., 2017. Dynamic homogenization theory for nonlocal acoustic metamaterials. Extreme Mech. Lett. 12, 71–76. URL: http://www.sciencedirect.com/science/article/pii/S2352431616300979, doi:10.1016/j.eml.2016.10.006.

Sagotra, A.K., Chu, D., Cazorla, C., 2019. Influence of lattice dynamics on lithium-ion conductivity: A first-principles study. Phys. Rev. Materials 3, 035405. doi:10.1103/PhysRevMaterials.3.035405.

Shmuel, G., Willis, J.R., 2025. Thermally bianisotropic metamaterials induced by spatial asymmetry. Phys. Rev. Lett. 135, 116303. doi:10.1103/tx76-hshd.

Shmuel, G., Willis, J.R., 2026a. Exact homogenization method for heat conduction. Phys. Rev. Applied 25, 014072. doi:10.1103/rgg3-19pc.

Shmuel, G., Willis, J.R., 2026b. Multiphysics bianisotropy in wave–diffusion metamaterials. Under review.

Sieck, C.F., Alù, A., Haberman, M.R., 2017. Origins of Willis coupling and acoustic bianisotropy in acoustic metamaterials through source-driven homogenization. Phys. Rev. B 96, 104303. doi:10.1103/PhysRevB.96.104303.

Srivastava, A., 2015. Elastic metamaterials and dynamic homogenization: a review. Int. J. Smart Nano Mater. 6, 41–60.

Torrent, D., Poncelet, O., Batsale, J.C., 2018. Nonreciprocal thermal material by spatiotemporal modulation. Phys. Rev. Lett. 120, 125501. doi:10.1103/PhysRevLett.120.125501.

Willis, J.R., 1981. Variational principles for dynamic problems for inhomogeneous elastic media. Wave Motion 3, 1–11. URL: http://www.sciencedirect.com/science/article/pii/0165212581900081, doi:10.1016/0165-2125(81)90008-1.

Willis, J.R., 1985. The nonlocal influence of density variations in a composite. Int. J. Solids Struct. 21, 805–817. doi:10.1016/0020-7683(85)90084-8.

Willis, J.R., 1997. Dynamics of composites, in: Suquet, P. (Ed.), Continuum Micromechanics. Springer, Vienna. volume 377 of *CISM International Centre for Mechanical Sciences*, pp. 265–290. doi:10.1007/978-3-7091-2662-2_5.

Willis, J.R., 2011. Effective constitutive relations for waves in composites and metamaterials. Proc. R. Soc. A 467, 1865–1879. doi:10.1098/rspa.2010.0620.

Wu, C., Shmuel, G., Yin, H., . Nonlocal thermal Willis coupling in laminated conductors. arXiv:2605.16983.

Xu, L., Xu, G., Li, J., Li, Y., Huang, J., Qiu, C.W., 2022. Thermal Willis coupling in spatiotemporal diffusive metamaterials. Phys. Rev. Lett. 129, 155901. doi:10.1103/PhysRevLett.129.155901.

Yves, S., Fruchart, M., Fleury, R., Shmuel, G., Vitelli, V., Haberman, M.R., Alù, A., 2026. Symmetry-driven artificial phononic media. Nat. Rev. Mater. 11, 156–180. doi:10.1038/s41578-025-00860-9.